Synthesis, Characterization and Photocatalytic Applications of Metal Doped Titania Nanoparticles

Author

Zubia Abid

NUST201463893MSCME67914

DEPARTMENT OF MATERIALS ENGINEERING

SCHOOL OF CHEMICAL AND MATERIALS ENGINEERING

NATIONAL UNIVERSITY OF SCIENCES AND TECHNOLOGY

ISLAMABAD

2016

Synthesis, Characterization and Photocatalytic Applications of Metal Doped Titania Nanoparticles

Author

Zubia Abid

NUST201463893MSCME67914

A thesis submitted in partial fulfillment of the requirements for the degree of
MS Nanoscience and Engineering

Thesis Supervisor:

Dr. Muhammad Israr Qadir

Thesis Supervisor's Signature:_____

DEPARTMENT OF MATERIALS ENGINEERING

SCHOOL OF CHEMICAL AND MATERIALS ENGINEERING

NATIONAL UNIVERSITY OF SCIENCES AND TECHNOLOGY

ISLAMABAD

2016

Thesis Submission Certificate

It is to certify that work in this thesis has been carried out by **Zubia Abid** and completed under my supervision in school of Chemical and Materials engineering, National University of Sciences and Technology, H-12, Islamabad, Pakistan.

MS-Supervisor

Dr. Muhammad Israr Qadir

Submitted through

Principal/Dean

School of Chemical and Materials Engineering Department

National University of Sciences and Technology, Islamabad

Dedicated to my exceptional parents and husband whose tremendous support and cooperation led me to this wonderful accomplishment…

Acknowledgements

Abstract

Titanium dioxide (TiO$_2$) has got a lot of attention due to its high photocatalytic activity hence use for water purification. It is non-toxic and insoluble in water. In present research the pure, singly doped (Zn and Ag) and co-doped (Zn/Ag) TiO$_2$ nanoparticles with molar concentrations 1, 3, 5 mol% have been synthesized by wel known wet chemical route, sol-gel. The photocatalytic activity of these nanoparticles have been scrutinized by using two commonly used textile dyes eosin y and methyl orange. XRD analysis showed pure anatase phase of TiO$_2$. Particles have uniform spherical morphology with size up to 20nm has been achieved. By FTIR analysis reveals successful doping into host matrix single band towards lower wavenumber. The UV/Vis analysis confirms the shift in bandgap towards the higher wavelength which indicate low bandgap energy required to initiate chemical reaction. Both dyes were tested at pH˜ 3 under UV-lamps. It was examined that 3 mol% Zn/Ag co-doped sample shows best photocatalytic activity towards both dyes as compared pure and singly doped TiO$_2$.

Table of Contents

List of Figures

List of Tables

List of Symbols

S = Surface area

V = Volume

r = Radius

Å = Angstrom

eV = Electron volt

cm = Centimeter

g = Gram

h = Plank's constant

c = Speed of light

λ = Wavelength

ϵ = Molar extinction coefficient

β = Full width half maxim

α = Absorption coefficient

hν = Photon energy

Chapter 1

Introduction

On 29th December 1959, at American physical society meeting, an innovative lecture delivered by Richard Feynman, "There is plenty of room at the bottom" i.e., manipulating things at smaller scale, opened a platform for researchers to unroll their imaginations [1]. He asked, "What would the properties of materials be if we could really arrange the atoms the way we want them?"[2]. Nanotechnology is getting much attentions because of its capability to forge novel assemblies at atomic gauge [3]. Nanotechnology is a spacious term indicating the phenomena's occurring at a gauge known as one billionth of a meter i.e., nanoscale as presented in Fig. 1.
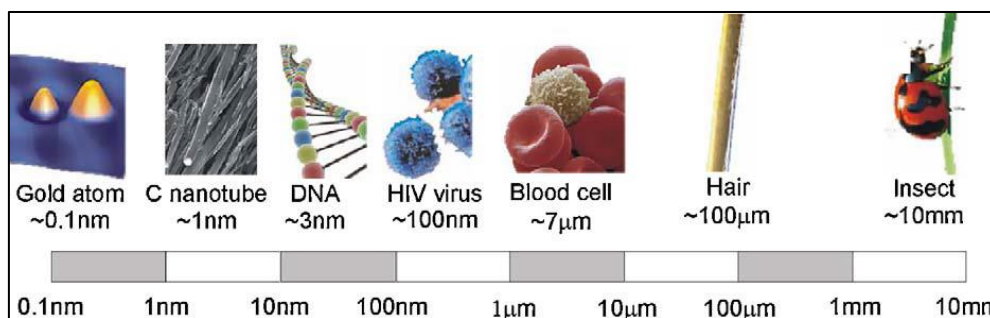
Figure 1.1- Length Scale and some related examples [3].

$$1 \text{ nm} = 10^{-3}\mu\text{m} = 10^{-6}\text{mm} = 10^{-9}\text{m}$$

So one can say, a nanometer (nm) or 10^{-9}m represents just few atoms or molecules [4]. The terminology "nanotechnology'' was first used by Norio Taniguchi in one of his paper on basic concepts in nanotechnology in 1974 [5]. Nanoscience and nanotechnology are new leading edges of this era, dealing with primitive interpretation and technical fees for manipulation of novel characteristics for the structures having size between 1-100nm.

The factors that differentiate nanoscale materials (nanomaterials) and bulk are surface to volume ratio and quantum confinement effects [6] .

a. Surface area to volume ratio (S/V)

By decreasing size of particles surface to volume ratio increases i.e., it has very large values for nanomaterials. Relation to calculate S/V ratio is given as, for a sphere we have,

$$\frac{Surface\ Area\ of\ Sphere}{Volume\ of\ Sphere} = 3/r$$

The sphere radius decreases S/V ratio increases. Nanomaterials as compared to bulk have large surface area to volume ratio. That's why some inert materials are highly reactive when their dimensions are in nanoscale e.g., gold nanoparticles.

b. Quantum confinement effects

According to energy bandgap theory, nanomaterials have bandgap between solid materials and isolated atoms. If dimensions of potential well are of the order of de-Broglie wavelength or mean free path of electron then energy level of electrons changes and electron will remain confined in small region of material [7]. This phenomenon is known as quantum confinement.

As size decreases energy of electrons change that's why quantum effects are pronounced in nanomaterials.

1.1 Classification of Nanomaterials

Nanomaterials have different shapes and sizes due to confinement in particular direction. Metals, semiconductors, polymers and ceramics every kind of nanomaterials can be obtained. The term nanocrystal was first used by Gleiter [8]. Classification of nanomaterials based on different parameters is given in Table 1.1.

Table 1.1- Classification of nanomaterials [9]

Classification	Examples
Dimensions	
• 3 D < 100nm	Particles, Quantum dots, Hallow spheres
• 2 D < 100nm	Tubes, Fibers, Wires, Platelets
• 1 D < 100nm	Films Coatings, Multilayers
Phase Composition	
• Single-phase solids	Crystalline, Amorphous, Layers
• Multi-phase solids	Matrix composites, Coated particles
• Multi-phase systems	Colloids, Aerogels, Ferro fluids
Manufacturing Process	
• Gas-phase reactions	Flame synthesis, Condensation, CVD etc.
• Liquid-phase reactions	Sol-gel, precipitation, hydrothermal processing etc.
• Mechanical procedures	Ball milling, Plastic deformation etc.

1.2 Applications of Nanomaterials

Nanotechnology is a burgeoning technology having applications in almost every field [10] e.g., agriculture and food system [11], chemistry and environment [12], information and communication [13], electronics [14], pharmaceuticals [15], energy [3] and photocatalysis [16]. Few applications are listed below in detail.

Table 1.2- Applications of nanotechnology in various fields.

Applications of Nanomaterials	
Nanomaterials for energy applications	- Energy conversion & storage - Solar cell - Li-ion battery
Nanomaterials for adsorption and catalysis	- Water treatment - Photocatalysis - Sensor
Single molecule and molecular nanostructures	- Molecule materials - Nanodevices - SPM
Recognition and interaction of biomolecules	Diseases diagnose & treatment
Drug delivery and pharmaceuticals	- Doxil and abraxane nanoparticles for cancer treatment [17] - Silver nanoparticles for healing of wounds [18] - CNTs and Bucky balls used as drug delivery vehicle [15]
Textile Industry	Titania nanocomposites coated fabrics provide shielding against bacteria [19]

1.3 Titanium Dioxide (TiO$_2$)

TiO$_2$ also had identified as Titania and Titanium (IV) oxide, oxide of naturally occurring transition metal Titanium (Ti) thus TiO$_2$ is a transition metal oxide. Ti is ninth most abundant metal on earth crust but in nature don't exist in metallic form. Ti was discovered in 1971 by R. William G. who showed the existence of a new element in the ore of ilmenite. In TiO$_2$,

conduction and valence band consists of filled 3d, 4s, 4p orbitals of Ti and 2p orbitals of Oxygen (O_2). Ti have three oxidation states 2^+, 3^+ and 4^+ among them 4^+ is most common.

TiO$_2$ (molar mass: 79.9g/mol) is insoluble, nonflammable and inodorous white powder having relative density of 4.26g/cm^3, boil over at 3245K and melts at 2116K TiO$_2$ shows eminent thermal, mechanical and chemical stability [20], along with high refractive index [21], low cost [22], nontoxic material [23, 24] and have several applications in various fields. TiO$_2$ has different polymorphs and are disused below.

1.3.1 Polymorphs of TiO$_2$

At atmospheric pressure TiO$_2$ has three naturally occurring polymorphs including anatase, rutile and brookite [25]. Among them rutile is most stable while anatase and brookite are metastable. Different crystallographic properties of these phases are given in table1.3:

Table 1.3- Crystallographic properties of TiO$_2$ polymorphs [26-28]

Sr. No.	Properties	Anatase	Rutile	Brookite
1	Crystalline Anatomy	Tetragonal	Tetragonal	Orthorhombic
2	Lattice Constant (Å)	a = 3.748 c = 9.515	a = 4.5936 c = 2.5987	a = 9.184 b = 5.447 c = 5.154
3	Wide Band Gaps (eV)	3.2 [29]	3.02 [29]	2.96 [29]
	Light Wave Length Threshold (nm)	384	410	401
3	Cell (Molecule)	2	2	4
4	Space Group	I4$_1$/amd	P4$_2$/mnm	Pbca
5	Density (g/cm^3)	3.79	4.13	3.99
6	Volume/Molecule (Å)	34.061	31.2160	32.172
7	O-Ti-O Bond Angle	77.7^o 92.6^o	81.2^o 90.0^o	77.0^o-105°
8	Ti-O Bond Length (Å)	1.937(4) 1.956(2)	1.949(4) 1.980(2)	1.87-2.04
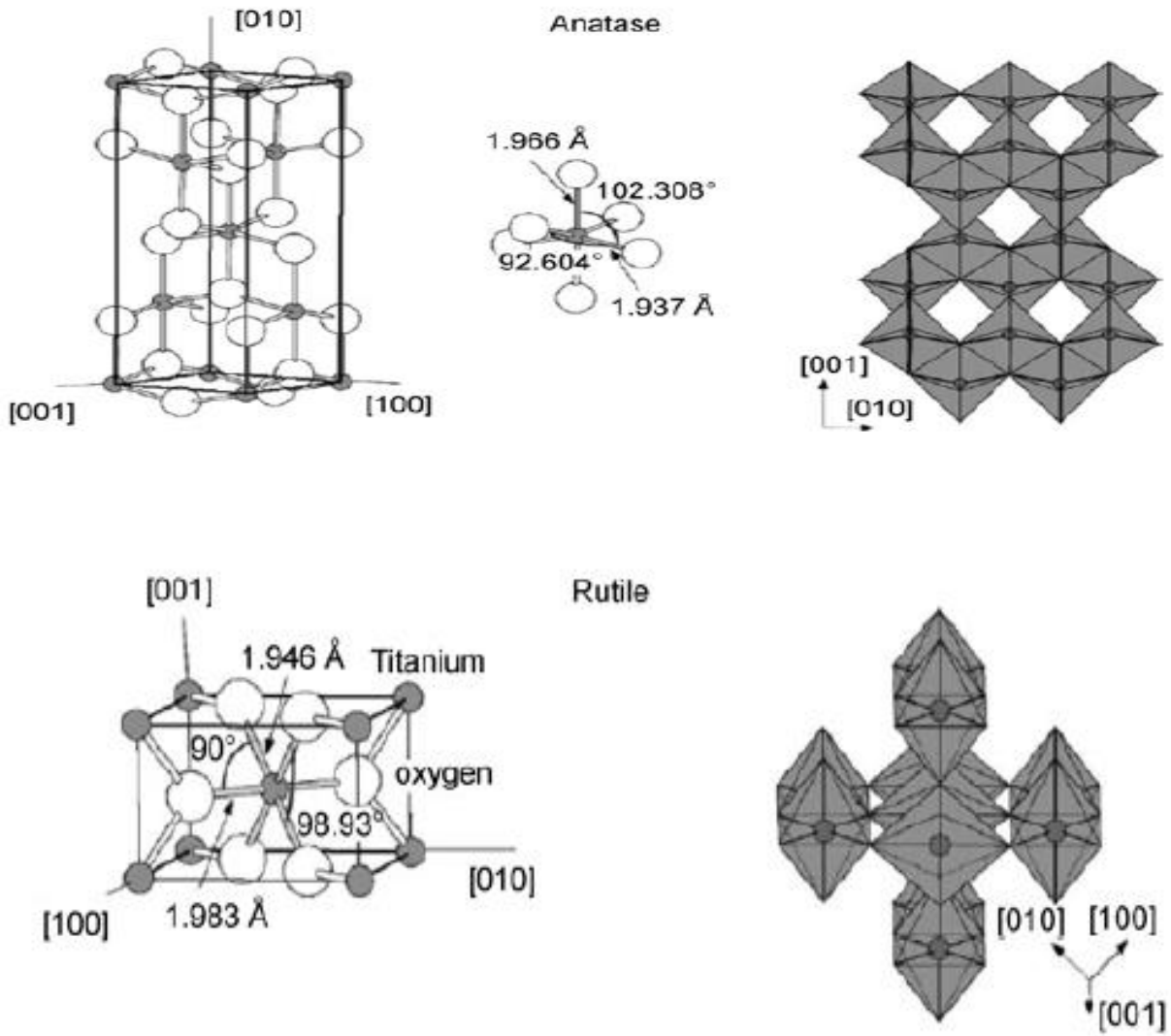
Figure 1.2- Crystal structure of anatase and rutile [30, 31]
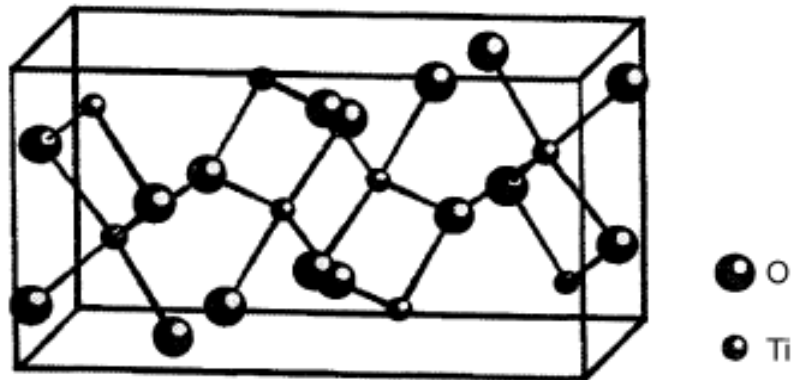
Figure 1.3- Lattice structure of brookite [28, 30].

It has been reported that other five phases of TiO_2 also exist at high pressure [32, 33]. These high pressure phases are also stable and reported [34-37].

1.3.2 TiO₂ applications

TiO_2 has number of applications in various fields depending upon its structure and phase. Some of them are elaborated below:

- Titania being white pigment has lot of uses in paints, polymers, toothpastes, medicines and in other materials where colorization is required [38].
- In heterogeneous catalysis, TiO_2 is mixed with Vanadium (V) oxide thus vanadia/titania catalyst is used for selective oxidation reactions [39]. vanadium (V) oxide is also a renowned catalyst.
- TiO_2 have numerous applications as sensor like titania films was successfully tested for different concentrations of methanol, ethanol and n-propanol gases at room temperature within 1min 80s [40].
- TiO_2 is perfect candidate for solar cell applications, for the high yield of H_2 [41] and power-driven applications [42].
- TiO_2 corrosion- protective coatings are used on large scale as an alternative to chromate based coatings and have given best results as test by electrochemical impedance spectroscopy (EIS) [43].
- To reach the sensitivity of next generation interferometric gravitational wave detectors, its necessary to reduce the noise from optical coatings that has been satisfied by TiO_2 doped Ta_2O_5/SiO_2 [44].
- Anatase TiO_2 50nm thick layer showed ohmic conduction due to partial depletion of carriers from the crystallites [45].
- Mesoporous TiO_2 owing large S/V ratio and number of active porous sites have gained much attention in photocatalysis and solar spectra transformation [46]. Photocatalysis is the most pronounced property of TiO_2.

1.4 Photocatalysis

Photocatalysis is termed as driving a chemical reaction in the presence of photocatalyst, catalyst thermodynamically favor the completion of reaction with low activation energy as shown in figure 1.4. Although catalyst speeds up the reaction but don't consume

throughout the reaction and can be recovered subsequently. Many transition metals and their complexes are used as catalyst like Ti, Fe, Pd, Pt, V etc.
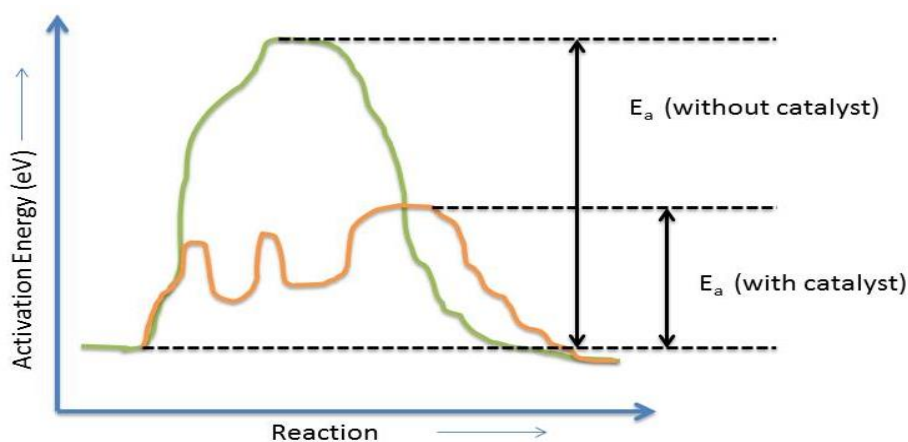
Figure 1.4- Schematic representation of catalytic and noncatalytic reactions

Salomon et al. [47] described the mechanism photocatalysis in detail. They reported that two main steps involved during photocatalysis which are:

i. Photogenerated catalysis

This is a catalytic step involving, thermodynamically spontaneous reaction proceeds when light interact with stable catalyst and excite it, simultaneously excited catalyst react with low energy substrate. It is also known as photo initiated catalytic reaction or photo-induce catalytic reaction.

ii. Catalyzed photolysis

Now both catalyst and substrate are in excited state now further light is used to increase the efficiency of reaction. This step is same as photo assisted catalysis or photosensitization.

So one can say light in the form of photons is used to initiate the photocatalytic reaction and electromagnetic spectrum is utilized as activation energy source. The relation between energy E of photons and wavelength λ of light is given by Plank's equation:

$$E = \frac{hc}{\lambda}$$

Here

8

c = speed of light $\quad\quad\quad\quad\quad\quad\quad\quad$ h = is plank's constant

Sakai *et. al.,* [48] reported main steps occurring during photocatalysis which are as under:

a) Photon absorption and e^-/h^+ inception
b) Oxidation of donor
c) Reduction of acceptor
d) Recombination of e^-/h^+ at surface

Oxidation-reduction are basic steps involved in photocatalysis. Whole mechanism is illustrated in schematic below:
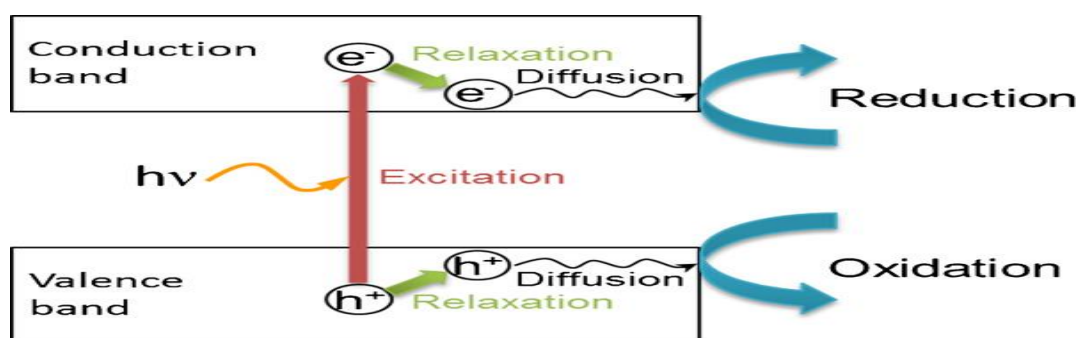
Figure 1.5- Photocatalysis schematic [16]

Photocatalysis have got attention in recent years, soon after the discovery of splitting of water reported by Honda and Fujishima [49]. Photocatalysis have number of applications in various fields especially in environment and energy related fields. A photocatalyst convert solar energy to chemical energy and oxidize or reduce the materials resulting in useful hydrocarbons [50-52], which further decomposes the harmful bacteria's and pollutants[16, 53, 54] in air and water [55-57]. TiO_2 is best known photocatalyst due to its strong oxidizing ability [58, 59] towards degradation of organic waste [56, 60], chemical stability, super-hydrophobicity[61], non-toxic, limpidity towards visible light and low cost.

1.4.1 TiO_2 as a photocatalyst

TiO_2 is best known photocatalyst due to high rate of radicles adsorption on its surface [62-65]. Ohtani et al. [66] reported that high photocatalytic of TiO_2 is based on its large surface area that absorbs pollutant and high crystallinity that reduces e^-/h^+ recombination. The first most important discovery after which photocatalysis is been promoted was "Honda-

Fujishima Effect" in 1972 reported by K. Honda and A. Fujishima, photolysis of water using TiO$_2$ electrode [49].

Among all low bandgap, stable and metastable phases of TiO$_2$, anatase has inherent high photocatalytic activity depending on chemical properties, high density of localized states [67] and low e-/h+ recombination [32] and low capacity to adsorb oxygen versus high hydroxylation because of high fermi level [68]. Some of the basic properties of anatase are enlisted in table 1.4 below:

Table 1.4- Properties of anatase TiO$_2$ [32]

Properties	Anatase
Crystal Structure	Tetragonal [69, 70]
No. of Atoms in Unit Cell (Z)	4 [71]
Lattice Constants (nm)	$a = 0.3785$ [71] $c = 0.9514$
Density (Kgm^{-3})	3894 [71]
Space group	$I\frac{4}{a}md$ [72]
Unit Cell Volume (nm^3)^a	0.1363 [32]
Refractive Index	2.54, 2.49 [38]
Experimentally Calculated Bandgap (eV)	3.2 [73-75]
Calculated Indirect Bandgap (eV)	3.23-3.59 [75]
Solubility in H$_2$O	Insoluble [38]
Solubility in HF	Soluble [76]
Bulk Modulus (GPa)	183 [77]
Hardness (Mohns)	5.5-6 [78]

The crystal structure of anatase is same as ruitle, the only difference is instead of sharing four corner octahedral shares four edges [79]. Low photocatalytic activity of rutile is due to its tightly packed structure and less defect sites.

1.4.1.1 Mechanism of photocatalysis in anatase TiO_2

As explained above photocatalytic activity of TiO_2 is due to adsorption of radicles on TiO_2 surfaces. When photons having energy equal or more than TiO_2 bandgap are directed towards TiO_2 surface electron hole pair is formed.

$$TiO_2 + h\nu \rightarrow h^+ + e^-$$
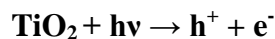
Superoxide anion ($^\bullet O_2^-$) is formed when electrons ejected from TiO_2 react with atmospheric oxygen.

$$e^- + O_2 \rightarrow {}^\bullet O_2^-$$
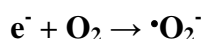
Moreover surface of TiO_2 which is positively charged absorbs moisture in the air; the moisture after losing electron becomes hydroxyl radicle ($^\bullet OH$).

$$h^+ + H_2O \rightarrow H^+ + OH^-$$

$$h^+ + OH^- \rightarrow {}^\bullet OH$$
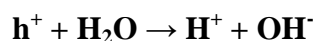
These radicles are atomic species having free electrons. These $^\bullet O_2^-$ and $^\bullet OH$ by their power of oxidation reduction decomposes unwanted bacteria's, organic chemicals hazardous materials etc. During this reaction two competing phenomena's occur i.e., e^-/h^+ generation and recombination [80].

1.5 Doping

The main drawback include for limiting the photocatalytic efficiency of catalyst is e^-/h^+ recombination [81]. There are several strategies to limit this problem and increase photocatalytic activity, including doping [82, 83]. Reduction of bandgap or introduction of trapping states is the main objective behind doping which sequels in the absorption of visible light. It's important to maintain the crystal structure of parent element during doping.

Doping is an important parameter to change response of photocatalyst that can be done by both organic and inorganic species but in present work we are interested in TiO_2 doping by metallic species. The variance in radicles charge and ionic radii it's easier to dope TiO_2 with cations [84]. Doping with metallic species is one of the routes to limit the charge carrier's recombination. These metallic species act as an electron trapping sump and charge

carriers life time increases which ultimately increases the photocatalytic activity i.e. by changing surface properties of TiO_2 catalyst [85].

It has also been reported that for doped TiO_2 photocatalytic activity doping ions amount and valence both are important factors [86]. When TiO_2 is doped with transition metal cations an electronic coupling effect induces which promotes the formation of electron states, these localized states are explained by Jasra et al [87]. The localized states can shift towards maximum of valence band or minimum of conduction band, if latter has been happened then carrier's life time increases and recombination limits. Joshi et al. [88] reported that by doping when TiO_2 is doped with transition metal cations the localized d-states form in the bandgap TiO_2. Shockley-Read-Hall (SRH) model further elaborates that these localized states act as trapping states and trap holes from valance band and electrons from conduction band and enhances recombination [89]. TiO_2 has been doped by number of transition metals [90-93].

Oxidation of different species is kinetically different. Minority charge carrier's diffusion length greatly affects the photoactivity of any material [91]. The space charge layer must have potential difference of 0.2V for maximum e^-/h^+ extraction [94]. Dopant concentration and its influence on e^-/h^+ recombination are calculated by equation below:

$$W = \frac{2\varepsilon\varepsilon_0 V_0}{eN_d}$$

Where

W= thickness of space charge layer ε= static dielectric constant of semiconductor

ε_0 = static dielectric constant in vacuum V_0= surface potential

 e= electron charge N_d= number of dopant donor atoms .

From above equation it is clear when amount of dopant is increased thickness of space charged layer decreases so e/h separation can easily done by electric field before recombination. As we go on increasing doping concentrations the thickness of space charge layer goes on decreasing and if there is no external driving force, the recombination of charge carriers becomes more frequent [30]. The photocatalytic degradation of RhB by Fe^{3+} doped TiO_2 is pronounced at low doping concentration [95].

Doping is independent of method adopt, many controversial results are reported in literature concerning this act [96]. Due to inherent lattice strain surface modification of nano-TiO_2 is more beneficial than bulk [97].

1.5.1 Co-doping

Co-doping is another improved form of doping which includes more than one dopant. Co-doping greatly enhances the photocatalytic activity by increasing charge separation and reduces recombination. Due to large reduction in bandgap TiO_2 photocatalyst becomes more efficient and able to absorb large sun spectra. Behnajady and Eskandarloo reported the comparison of photocatalytic activity of Ag/ TiO_2, Cu/ TiO_2, and Ag,Cu/ TiO_2, reports shows codoped sample have high photocatalytic activity as compared to mono-doped samples and pure sample [98].

Ag and Cu both have their positive effects to increase photocatalytic activity if TiO_2. Fermi level of Ag lie below the conduction band of TiO_2, when light falls on TiO_2 catalyst surface e/h pair generates, electrons jump to the Ag metal because of the formation of Schokely barrier at contact region of Ag-TiO_2. Theses electrons combine to atmospheric oxygen and results in the formation of superoxide anion (O^{-2}) also holes in conduction band combine with water to produce hydroxyl radical (OH-) in this way recombination is reduced. The reduction potiential of Cu is higher than TiO_2 thus capturing the photo-produced electrons it reduces the e/h recombination resulting in high photocatalytic efficiency.

1.5.2 Phase transformation

TiO_2 has three commonly known polymorphs among them rutile is thermodynamically stable at ambient pressure and temperatures while others are metastable. Both metastable forms transform on heating to rutile [99]. Thermodynamically anatase to rutile phase transformation is an irreversible process and is important for several applications including photocatalysis, pigments, electronics and sensors [100]. Phase transformation in TiO_2 depends on several factors including:

- Defects concentration [101]
- Grain boundary concentration [102]
- Particle packing [103]
- Doping [104]

- Alternating temperature [105]
- Changing pressure [106]

In detail doping and temperature effects has been discussed. The ease of transformation anatase to rutile is due to less constrained molecular construction [107].

1.5.2.1 Phase transformation by doping

Doping is essential to enhance the photocatalytic activity of TiO_2 photocatalyst. Generally the purpose of doping is to:

- Reduce bandgap [108]
- Improve e^-/h^+ separation [109]
- Escalation in level of superficial adsorbed species [110]
- Introduction of mid gap states [111]

Several reports have been submitted that ensures the effect of doping on phase transformation. It has been noticed that unintentional doping and impurities cause great change in phase transformation [112]. Heterogeneous nucleation is supported by precipitation due to increased solubility of impurities and dopants [113, 114].

Doping has been done by both cations and anions and numerous effects have been studied. Cations with low valence or small radii have showed phase transformation to rutile due increase in oxygen vacancies [101, 115, 116]. On the other hand, cations with valence higher 4 showed resistance towards the phase transformation. Table 1.5 shows the detail of some phase promotor/inhibitors cations dopants reported in literature.

Table 1.5- Effects of dopant on phase transformation of TiO_2

Sr. No.	Phase Transform Promotors		Phase Transform Inhibitors	
	Cation	**Dopant Phase Used**	**Cation**	**Dopant Phase Used**
1	Zn	ZnO [117]	Fe	$FeCl_2$ [113]
2	Cr	$CrCl_3$ [118]	Au	$HAuCl_4$ [119]
3	Cu	CuO [115, 120]	Ce	CeO_2 [121]
4	V	VO_2 [122], V_2O_5 [123]	Eu	$EuCl_3$ [124], Eu_2O_3 [111]
5	Sb	Sb_2O_3 [125]	Si	$Si(OC_2H_5)_4$ [126, 127],

				SiCl$_4$ [116, 128]
6	Sn	SnCl$_2$ [129] SnO$_2$ [130]	Sr	Sr(NO$_3$)$_2$ [116]
7	Al	AlCl$_3$ [131]	Al	AlOOH [132], AlCl$_3$ [133]
8	Ni	Ni(NO$_3$)$_2$ [122]	Y	Y$_2$O$_3$ [134]
9	Mn	MnO$_2$ [135], MnSO$_4$ [114], Mn(NO$_3$)$_2$ [136]	La	La$_2$O$_3$ [116]
10	Li	LiF [137]	Ca	Ca(NO$_3$)$_2$ [116]

1.5.2.2 Phase transformation by heating

At all temperatures anatase is less stable [138-140] and its transformation to rutile has been investigated at different transition temperatures. Generally it is assumed that transformation occurs at 600°C to 700°C [105]. Studying the effect of calcination temperature on phase transformation shows that below 600°C there is complete anatase phase above this temperature phase transformation occurs. At 600°C to 650°C there is complete transformation in rutile phase. After 750°C rutile change phase to anatase and mixed phase obtain at that point.

1.6 Applications of TiO$_2$ as a photocatalyst

TiO$_2$ Photocatalyst has huge number of applications in almost every field. This versatile photocatalyst has advance use in solar cells based industries for the assembly of H$_2$ and electricity. In heterogeneous catalysis it is used as a gas sensor, corrosion shielding glaze, pigment, in electrical devices and ceramics.
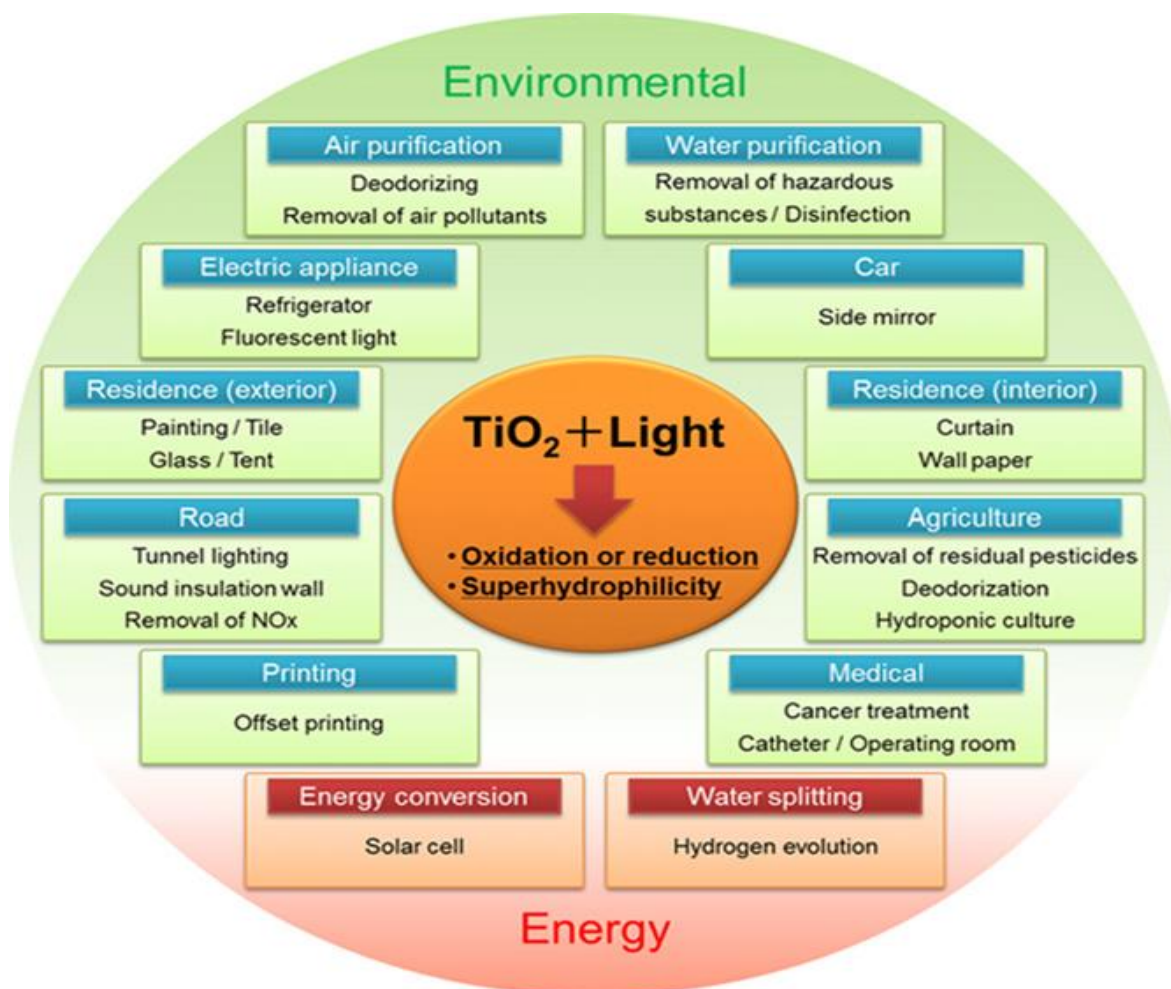
Figure 1.6- Applications of TiO$_2$ Photocatalyst [16].

1.6.1 Waste water treatment

Clean water means water free of pathogens and toxic materials is the key need of this era. The main problem facing for the production of clean water due to decreasing number of fresh water supplies because of several reasons including; population growth, extended droughts, competing demands of variety of users and more straight health based regulations [141]. Water may have any type of hazardous elements that are dangerous to every kind of living organism on earth.

Recent advances in nanotechnology has reported lot of opportunities for the protection and recycling of water by degradation of pollutants. TiO$_2$ photocatalyst is one of the successful candidates for waste water treatment. It shows complete mineralization of several types of dyes, polymers, herbicides and pesticides, polymers and aromatics. These pollutants are degraded into CO$_2$, water and mineral acid at normal temperature and pressure

conditions. Immobilized system and suspension are two basic systems involved in the degradation using TiO_2 photocatalyst [142]. Suspension involves the separation and recycling of catalyst particles from treated waste water and can be a time consuming process to avoid such problems photocatalyst on a suitable support is used but it reduces the reaction rate by lowering the surface area of photocatalyst.

In textile and photographic industry waste water huge numbers of synthetic and other harmful dyes are present. Over last few years research has been focused to degradation of dyes in industrial waste water [46, 143-145]. It is well known that when light is fall on the surface of TiO_2 end products are $^{•}O_2^{-}$ and $^{•}OH$ that take part degradation of dyes as shown below [146]:

$$Dye + {}^{•}O_2^{-} + {}^{•}OH \rightarrow Degradation\ Products$$

$$Dye + h^{+} \rightarrow Oxidation\ Products$$

$$Dye + e^{-} \rightarrow Reduction\ Products$$
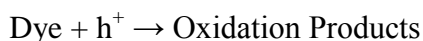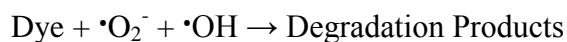
Both the species along with other oxidant species are responsible for TiO_2 photo-degradation of dyes. Dyeing is the major process in any textile or photographic industry, only few percent is used in process and huge amount is lost in water. Many of the dyes contain heavy metals like chromium, copper, sulfur etc. which are harmful to every kind of living specie. So cleaning of waste water is a big challenge of this era for the survival of each kind of kingdom on earth.

Chapter 2

Literature Review

In 1921, C. Renz [147] first time reported the photocatalytic behavior of TiO_2. In the presence of organic compounds such as glycerol, TiO_2 partially reduces and color changes to blue, grey and black also. He proposed a reaction for the reduction of TiO_2 via TiO_2 +light $\rightarrow$ Ti_2O_3 or TiO.

In 1938, Goodeve *et. al.,* [148] reported the quantum yields and absorption spectra of decomposition of dyes in air on TiO_2 powder on the basis of chalking phenomena in TiO_2. They declare TiO_2 as a catalyst for the acceleration of degradation reaction.

In 1949, Jacobsen [149] studied the chalking and photochemical reactivity correlation of TiO_2 pigment in paint named as cyclic redox process. The changes experienced by TiO_2 and paint are reversible and irreversible respectively thus CO_2 and water-soluble organic acids form. Due to chalking tendency TiO_2 powder undergoes the oxidation and then reduction mechanism in the presence of organic compounds. Discoloration takes place during reduction measured as loss of refractivity.

During the 1950s [150] ZnO materials got lot of attention as a photocatalyst. M. C. Markham *et. al.,* [151] and T.R. Rubin [152] reported the production of hydrogen peroxide (H_2O_2) when ZnO surface is illuminated in detail i.e., formation of radicles by transferring electrons to water shows photodecomposition basically also during the reaction atmospheric oxygen reduced and organic compounds are oxidized. The yield of H_2O_2 improved with the addition of organic compounds.

In 1953 M.C. Markham *et al.,* [151] and in 1956 R. E. Stephens [153] reported the large number of solid catalysts for the photo-production of H_2O_2 and the deserted TiO_2 because of very poor efficiency of photo-production. Because upon absorption of energy photolysis of crystal takes place even in the presence of organic compounds which shows the stability of next lower valance. They also showed that CdS have more tendencies for the photo-production of H_2O_2 as compared to ZnO.

In 1956 W.R. Hindson *et al.,* [154] reported effects of anatase pigment on strength of cotton fabric after one year exposure to sunlight, they have found that there is loss in strength by 25% due to actinic damage.

In 1958 D.R. Kennedy [155] studied the complete phenomena involved in photocatalysis i.e. electrons of TiO_2 are photo-excited they reduce adsorbed oxygen on TiO_2 surface. Ability of TiO_2 to photo-decompose the chlorazol sky blue is correlated to adsorbed oxygen.

In 1964 S. Kato et al. [156] found that anatase is more photoactive then rutile. They have used suspension of TiO_2 to oxidize hydrocarbons and alcohols simultaneously with the production of H_2O_2.

In 1972 most important breakthrough has been done in the ground of photocatalysis known as "Honda-Fujishima Effect" by K. Honda and A. Fujishima [49]. The process was photolysis of water by using rutile electrode immersed in an electrolyte with platinum (Pt) counter electrode. When rutile electrode is photo-illuminated evolution of oxygen takes place and evolution of hydrogen at counter electrode. The overall reaction is:

$$H_2O + 2h+ \rightarrow (1/2)O_2 + 2H^+$$

(at TiO_2 electrode)

$$TiO_2 + 2h\nu \rightarrow 2e^- + 2h^+$$

Absorption of light

$$2H^+ + 2e^- \rightarrow H_2$$

(at Pt electrode)
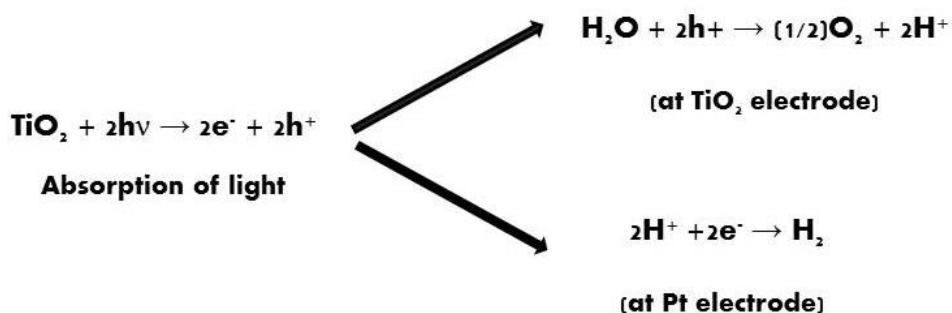
In 1977 N.S. Frank *et. al.,* [157] and N.G. Schrauzer [158] using "Honda-Fujishima Effect" reported the degradation of CN^- and molecular nitrogen (N_2) to ammonia (NH_3) and traces of hydrazine (N_2H_4) by TiO_2 and Fe-doped TiO_2 respectively. During formation of ammonia O_2 is released but H_2 inhibited due to formation of NH_3. Fe doping transforms anatase to rutile enhances the photocatalytic activity of rutile.

In 1985 Matasunaga et. al., [54] reported first time photochemical sterilization by platinium (Pt) loaded TiO_2. TiO_2/Pt catalyst show complete photo-killing behavior for E.coli, S. Cerevisiae and L.acidophilus for 60-120 min of UV irradiation. TiO_2/Pt oxidize the coenzyme in the cell which results in the complete inhibition of respiratory system and thus bacteria death.

19

In 1986 A. Fujishima *et. al.,* [159] reported photokilling of tumor cells by TiO_2 photocatalyst (HeLa cells).

In 1991, Regan and Gratzel [160] testified another remarkable discovery by using TiO_2 in dye-sensitized solar cells (DSSC). These DSSCs are low cost with high efficiency and harvest large solar spectrum. Cell consists of TiO_2 nanoparticles with organic chromophore groups. Cyclic redox reaction takes place in cell having high current density and exceptional stability. The light to electric energy conversion efficiency was 7.1-7.9% and 12% in stimulated sun light and in dispersed day light respectively.

In 1998 R. Wang *et. al.,* [161] reported excellent anti-fogging and self-cleaning characteristics of extremely hydrophobic TiO_2 surfaces.

In 2002 S. Watson *et. al.,* [162] reported a novel magnetic photocatalyst having magnetic core (Fe_3O_4/SiO_2) and TiO_2 shell synthesized by sol-gel. This catalyst can easily be removed from a slurry type of reactor by using peripheral magnetic field. Different coating techniques were first time applied on such catalyst and it was observed that direct coating if TiO_2 gives pure anatase phase and uniformly cover the magnetic seed. To improve the crystallinity of magnetic catalyst calcination is required.

In 2004 R.S. Sonawane *et. al.,* [163] reported TiO_2 films doped by iron (Fe) for the degradation of an industrial dye methyl orange (MO). Doped catalyst showed 2-2.5% high photocatalytic activity as compared to undoped and degrade almost 95% of MO after 3-4 hours exposure to sunlight. Fe doping increases the absorption of TiO_2 in visible region (400nm-800nm).

In 2008 S. Diamandescu *et. al.,* [164] reported codoped TiO_2 photocatalyst (Fe and Eu codoped) synthesized by hydrothermal method. The bandgap decreased from 2.9eV to 2.8eV for 1% codoped sample. Degradation of phenol by Fe/Eu codoped was remarkable. Fe doping no effect on metal-metal bond length while Eu increases the length and hence showed the little phase conversion anatase to rutile. Doped ions completely imbed into to the anatase lattice causing high photodegradation.

In 2009 lai *et. al.,* [165] reported cytotoxicity of folic acid modified TiO_2 towards cancer cells when illuminated. Folic acid was used to specify target due to presence of folate receptors on cancer cells. Surface modification of TiO_2 with folic acid decreases its photoactivity but increases the photo-killing of cancer cells (HeLa) upon UV illumination as compared to

unmodified TiO_2. The modified photocatalyst not only damage plasma membrane but also induce programing cell death. Flow cytometry based analysis shows that cell death is due to necrosis and apoptosis both.

O.R. Rocha $et.$ $al.,$ [166] used TiO_2 based hetero-catalyst for the treatment of oil sludge by photocatalysis. Heterogeneous photocatalysis showed efficient degradation and mineralization of organic compounds in the oil sludge. This catalyst has much efficient to remove 100% of polyaromatic hydrocarbons (PAH) after 96h of white light illumination. The removal of PAH is beneficial to humans and environment.

Chen $et.$ $al.,$ [167] studied photodegradation of methyl orange by Zn-doped TiO_2 photocatalyst synthesized by steric-acid gel method. The photocatalytic activity of bare and doped TiO_2 synthesized by steric sol gel process was much high as compared to sol-gel synthesized TiO_2 and P25. That was further confirmed by BET analysis; bare and doped TiO_2 has large surface area i.e., 91.25 and $152.0 m^2/g$ respectively. The optimal value for complete degradation was observed to be 0.1% Zn doping, by altering this value photodegradation decreases.

Zhao $et.$ $al.,$ [168] reported rhodamine B degradation by visible light irradiation by Zn-doped TiO_2 synthesized via hydrogen-oxygen diffusion flame method. Band gap decreases by incorporating Zn content because surface oxygen vacancies increased and introduce new sub-band levels below the conduction band of TiO_2 thus absorption edge shifted towards red. The optimal value calculated for maximum photocatalytic activity under visible irradiance for Zn doped TiO_2 is 0.37%.

Mirkhani $et.$ $al.,$ [169] reported complete photocatalytic degradation and mineralization of eight azo dyes by Ag doped TiO_2 under 400W high-pressure mercury lamp irradiance. Rate constant for TiO_2 was less than that of Ag doped TiO_2. Reaction obeys Langmuir-Hinshelwood model and pseudo first law shown by kinetic investigations. It was observed that 98-100% dyes were degraded by Ag doped TiO_2 in 30-150 min. The degradation increases till an optimal value of photocatalyst then decreased. Doping of Ag decreases the electron hole recombination, due to recombination degradation rate decreases. Reaction was also favourable at pH 8-9 and acidic medium.

W. Choi $et.$ $al.,$ [170] reported doping of quantum sized (2-4) TiO_2 colloids with 21 different metal ions. Among them 0.1%-0.5% doping of Fe, Ru, Mo, Os, Re, Rh and V showed

enhanced chemical reactivity towards the oxidation of $CHCl_3$ (degradation) and reduction of CCl_4 (dechlorination) whereas Al and Co decreases the photoreactivity. Steady-state photolysis quantum yield shows a correlation between doped quanta sized TiO_2 colloids and transitory recombination dynamics of e^-/h^+. Photoreactivity is observed to be increased with the trapped carrier's concentration.

M. M. Joshi *et. al.,* [88] reported that adversarial photocatalytic effect of TiO_2 by incorporating transition metal ions into TiO_2 matrix. The localized d-states formed in the bandgap of TiO_2, these d-states acts as trapping states and capture e^-/h^+. N-doping causes the production of localized p-states just above the valance state of TiO_2 thus band gap is reduced and photocatalytic activity is pronounced in visible region as compared to pure TiO_2. N-doped TiO_2 degrade methyl orange (MO) to hydrazine (N_2H_4) derivatives depending on the intensity of light, initial concentration and photocatalyst loading.

El-Bahy *et. al.,* [171] reported the TiO_2 doping by lanthanide series (La, Nd, Sm, Gd, Yb) by sol-gel. Among them Gd doped TiO has small particle size, lowest bandgap and highest surface area and pore volume. Lanthanides ions showed more photocatalytic activity as compared to pure TiO_2 but among them Gd doped TiO_2 was higly photocatalytic with 100% DB53 dye removal. The difference in photocatalytic activity is due to change in number of surface hydroxyl group.

Song *et. al.,* [82] reported Cu/N co-doped TiO_2 nanoparticles for the degradation of xylenol orange and revealing its application in organics degradation. Codoped photocatalyst was first time synthesized with extend absorption edge of TiO_2 to 590nm and showed highest photocatalytic activity as compared to pure, Cu and N doped TiO_2 due to narrowing of bandgap by mixing N 2p and O 2p states and inhibiting if carriers recombination due to Cu at the surface of TiO_2. This catalyst has potential applications for the degradation of organic pollutants.

J. Xu *et. al.,* [172] synthesized C/Ce co-doped photocatalyst by sol-gel to degrade "Reactive Brilliant Red X-3B" by visible light. Codoped photocatalyst showed pronounced degradation as compared to pure and mono-doped due to inhibition of e/h recombination and charge transfer by Ce 4f level. Appearance of new electronic states between bandgap of TiO_2 exhibits the red shift to visible region.

Z.X. Shen *et. al.,* [173] synthesized N/Ce codoped TiO_2 photocatalyst by sol-gel with high surface area for the degradation of nitrobenzene under visible light irradiation. N atoms incorporate into the lattice of TiO_2 and modify the electronic states below the conduction band edge hence decreasing the bandgap. Whereas Ce ions remain on the surface of TiO_2 inhibiting the e/h recombination having no contribution to band narrowing. Codoping showed efficient photo-degradation attributed to the synergistic effect. Codoped catalyst was found to be 175% more catalytic as compared to pure TiO_2 for the degrading nitrobenzene under visible light.

X. Yang *et. al.,* [174] synthesized codoped (Ag/V) TiO_2 by single step sol-gel solvothermal process using triblock copolymer. The synthesized three junction photocatalyst consists of mixed phase anatase and rutile with bandgap 2.25eV as V completely imbed into the TiO_2 lattice, having high photocatalytic activity for rhodamine B and Coomassie Brilliant Blue G-250 under UV-Vis irradiation as compared to pure and mono-doped sample. Metallic Ag remains spread on the surface of TiO_2 enhancing quantum efficiency high synergic effects appear by high absorption in visible region due to enhanced V doping. Ti-3d and V-3d hybridized to Ti-V conduction bands of TiO_2. Hybridized orbital have energy as compared to Ti 3d so red shifts appear when carriers transfer take place form O 2p to Ti-V 3d.

Wang *et. al.,* [175] synthesized Fe^{3+} doped TiO_2 nanoparticles by plasma oxidative pyrolysis with average particle size about 50-60nm. The aqueous suspension of doped catalyst was used to degrade methyl orange under UV/Vis illumination. The degradation of dye is greater under visible light as compared to UV because dopant induces intermediate bands and reduces band gap of TiO_2. The dye was completely degraded after 90min and reaction was pseudo- first order.

Yin *et. al.,* [176] reported the degradation of eosin Y and rhodamine B by P25 and mesoporous TiO_2. Degradation enhances when more dye molecules adsorbed on TiO_2 surface. The catalyst amount 50mg was suggested as optimal value for complete degradation and complete degradation of both dyes was observed in 35min. Superoxide anion and EDTA plays inverse role in degradation.

Saquib *et. al.,* [177] investegated the degradation of two dyes *i.e.,* eosin yellowish and *p-*rosaniline under various conditions including presence of different electron acceptors, pH change, concentration of substrate and catalyst and different types of TiO_2. The degradation increase at decreasing pH values, lower concentration of substrate and increasing amount of

catalyst. It was found that UV-100 catalyst was more efficient for eosin yellow degradation and P25 for *p*-rosaniline. Daughter elements after degradation were analyzed by GC/MS technique.

Taoda [178] developed a core shell structure i.e., silica beads coated with TiO_2. Because of large reaction area photocatalyst consents the effective decay of nasty odors, dyed matter and organic surplus present in waste water.

Bui *et. al.,* [179] reported complete mineralization of two azo dyes Reactive Red 4 and Black 5 from industrial waste water using powdered TiO_2 photocatalyst. N_2 has been established in photoreactor during degradation reaction and noticed that degradation was 100% by using inert atmosphere.

Prairie *et. al.,* [180] reported that depending on the standard reduction potential of metals TiO_2 has ability to remove certain numbers of metals from waste water. It has been demonstrated that metals having potentials more positive than 0.4V can easily catalyzed. Photoextracted conduction band electrons react readily with dissolved metal of proper reduction potential and reduce them on semiconductor surface. Waste water several types of metals were treated with 0.1 wt% TiO_2 photocatalyst under dark and UV irradiation, it was noticed that certain number of metals were removed even in dark but Cd and Ni were not removed.

Mahmoodi *et. al.,* [142] repoted the complete mineralization of AB 25 dye by using immobilized TiO_2 photocatalyst in a photocatalytic vessel. Restrained TiO_2 was capable of degrading and lessening the toxicity of dye. Daughter elements were carboxylic acid intermediates and organic compounds. Mineralization of AB 25 was done by producing nitrates and sulfates anions.

Pereira *et. al*., [181] reported maximum degradation of two xanthene based dyes *i.e.,* erythrosine B and eosin Y. Degradation was observed in photocatalytic chamber consists of aluminum plate slanted at 37° with surface working area. Degradation of dye in 24h fits to exponential decay curve representing fast first order reaction kinetics performed under acidic conditions. Toxicity analysis confirms that by products are less cytotoxic as compared to unreacted dye due the presence of bio transformational products, would be an efficient strategy for treatment of waste water.

Mohammadi et. al., synthesized Ag/Zn codoped TiO_2 nanoparticles by two different sol-gel techniques i.e., sol-gel synthesis under refluxing temperature in the presence of ethanol and low temperature sol-gel synthesis in the presence of acetic acid. The degradation of methyl orange was increased with codoped TiO_2 as compared to bare TiO_2 due to increase in total pore volume, surface area and decrease in crystallite size. Also sol-gel method has greater photocatalytic activity as compared to low temperature sol-gel method [182].

Chapter 3

Synthesis Techniques

Synthesis of nanomaterials has attracted attention for the past many years, now we have diverse techniques to synthesize nanomaterials. Synthesis of these dwarf materials highly influences the material properties including catalytic, electronic, mechanical, optical and optoelectronics. The most important factors that need to be address while developing synthesis techniques are simultaneous control over dimension, morphology and monodispersity [183]. Nanomaterials synthesis is divided into two basic categories one that starts with bulk materials (physical methods) and other that depends on the self-assembly of atoms (chemical methods). In physical methods control of size is difficult while in latter precision in size can be achieved easily.

Table 3.1: Synthesis techniques for nanomaterials

Bottom Up Techniques	Solution-Based Chemistry	▪ Sol-gel synthesis ▪ Hydrothermal Synthesis ▪ Electrophoretic deposition ▪ Heterogeneous/homogenous precipitation ▪ Sonochemical method ▪ Co-precipitation method ▪ Template-assisted synthesis ▪ Micro-emulsion method ▪ Electrochemical synthesis ▪ Solvothermal method
	PVD	▪ Thermal evaporation ▪ Pulsed LASER deposition ▪ Rf sputtering
	CVD	▪ Plasma enhanced CVD ▪ Thermal CVD ▪ Metal-organic CVD

		▪ Low pressure CVD
		▪ Atomic layer deposition (ALD)
		▪ Molecular beam epitaxy (MBE)
Top Down Techniques	Miscellaneous Methods	▪ Lithography
		▪ High energy ball milling

3.1 Sol-Gel

Sol-gel process indicates inorganic polymerization, also known as chameleon technology. The history of sol-gel process started in mid nineteenth century with the production of a monolithic glassy substance by a French chemist J. Ebelman. In 1846 Ebelman, leaving the mixture of tetraethylorthosilicate (TEOS) and water untouched, a silica glass like monolith was obtained after several months [184]. In 1864, Scottish chemist Thomas Graham observed phenomena; he was first who used the terms sol, gel and collide. Sol-gel technique comes of age between 1950-1970, when gelling properties of some other inorganic materials have discovered.

A low temperature solution based technique by which both crystalline (ceramics) and non-crystalline (glass like) materials can be synthesized by this process. Two basic steps involved in this process are: sol i.e., colloidal suspension through hydrolysis and gel i.e., polymerization of specific precursor into gel. Sol-gel is a diverse technique having many advantages over conventional methods for ceramics production; low cost, purity, low temperature processing, homogeneity, easy to synthesize variety of structures and control over properties [185]. The crystallinity of final product strongly depends on the reaction conditions used. According to Flory the term gel have diverse meaning that can be classified into four categories [186]:

    I.   Highly disordered polymer networks formed through physical aggregation

    II.   Well-ordered lamellar structure

    III.   Particular disordered structure

    IV.   Completely disordered covalent polymeric networks

Precursor is used as starting material; typical precursors are soluble organic or inorganic salts, colloidal sols, alkoxides and nitrates. The alkoxides route consists of metal alkoxides and non-alkoxide route utilizes salts such as chlorides, nitrates, carbonates, acetylacetonates,

acetates etc. Different type of powders, films and monoliths can be synthesized by sol-gel process. By using same starting material one can synthesize different materials. Drawback associated with non-alkoxide route is, solution require additional removal of anions. Alkoxides are commonly used precursor of sol-gel method.

Sol-gel material production involves seven steps:

Mixing

Casting

Gelating

Aging

Drying

Dehydration
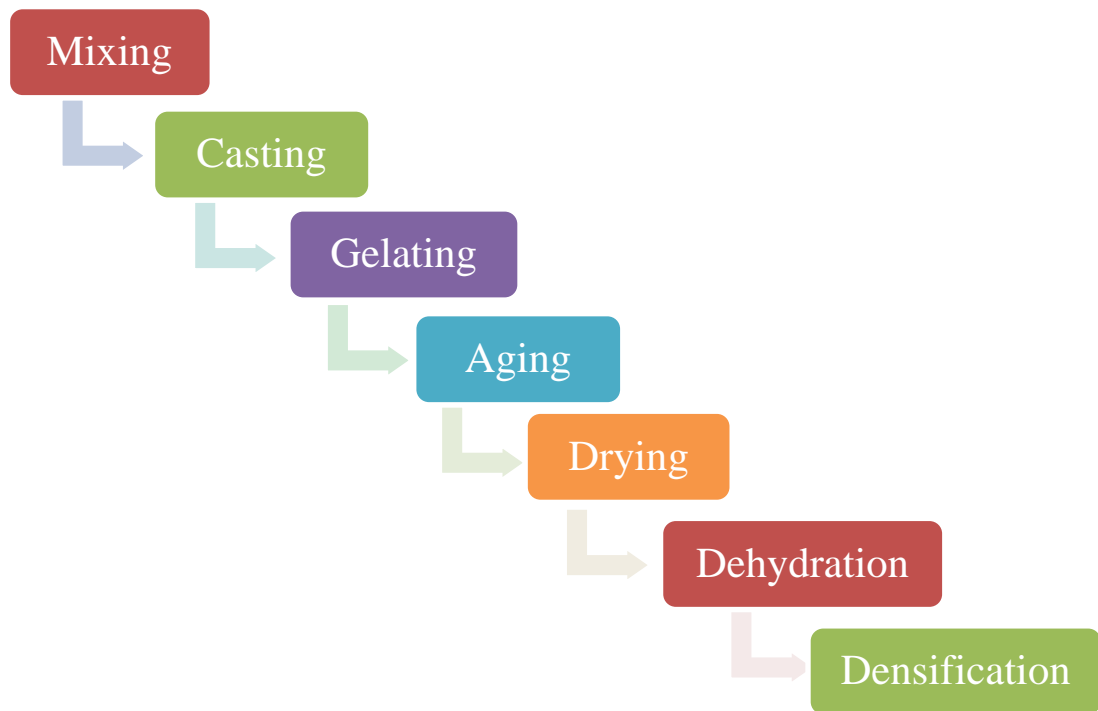
Densification

Among them mixing is key step to control the size and uniformity of the particles in the colloidal sol. When sol viscosity reaches a point called plateau (can support stress) it is known as gelation. For further solidification liquid is separated from gel by syneresis i.e., aging of gel. Most of the shrinkage of gel occurs during syneresis. At low temperatures strain experienced by gel is greater (flexible gel) but at elevated temperature stiffer structure is obtained due to fast condensation. The density and average pore size of gel depends on aging. Longer the aging period, stronger the monolith. Solvent is completely removed by drying, a point at which monolith experience maximum stress resulting in cracks. Cracking can be prevented by supercritical drying. A solid glassy structure with high density is obtained in the last by heating the dried solid up to 1100°C by densification.

Sol-gel schematic is shown in Fig 3.1. Xerogel is obtained when water and solvent are evaporated at room temperature. When water and solvent are removed as gas at elevated temperatures; 98% hollow pore volume with density up to 0.08% g/cm^3 is obtained known as

aerogel. These porous materials are further used as template for synthesis of other micro and nanoscale materials.
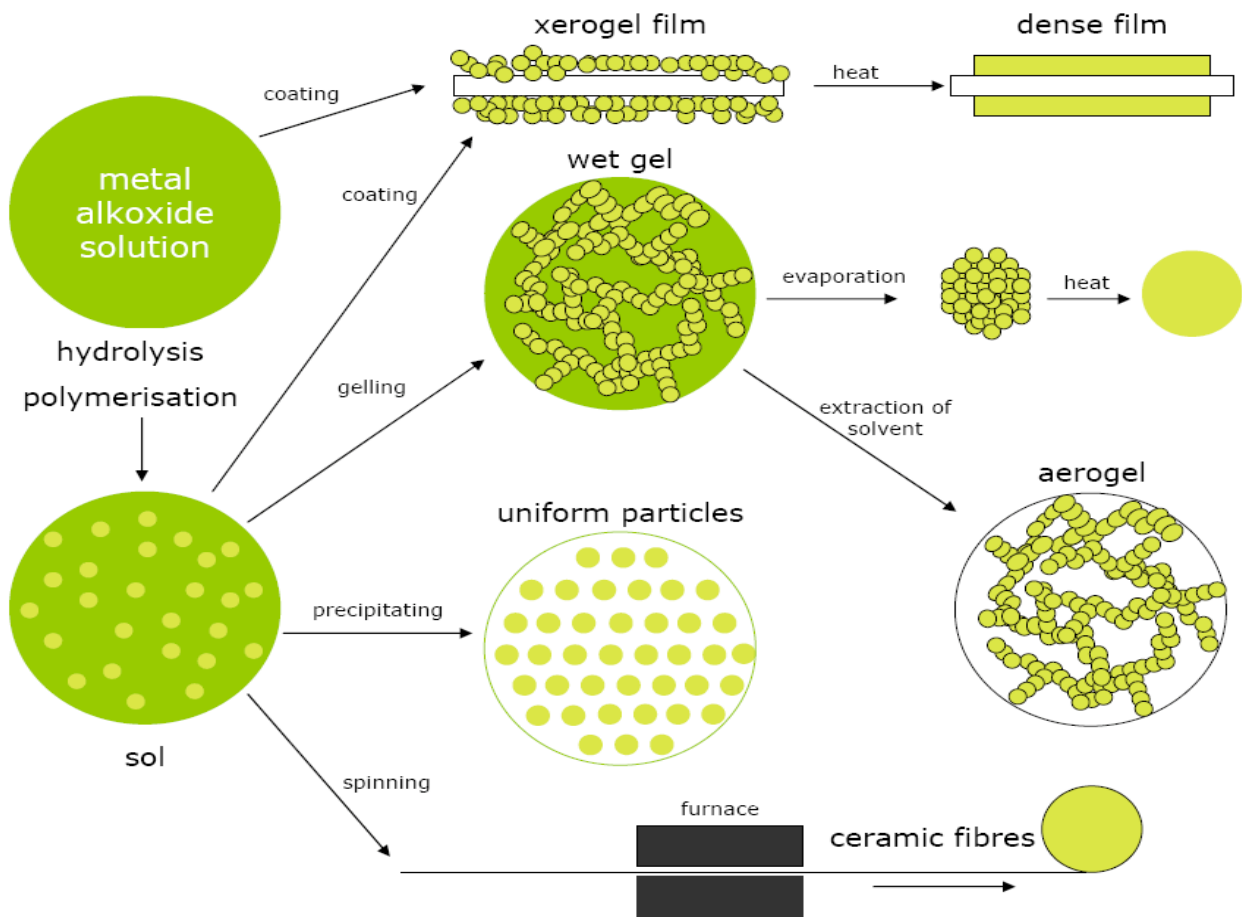

Figure 3.1- Schematic diagram for sol-gel process

3.1.1. Sol-gel chemistry

Sol-gel chemistry is based on two basic nucleophilic displacement reactions; hydrolysis (Olation) and condensation (Oxolation) followed by polymerization. The cross linking and degree of branching of inorganic polymer and later porosity of gel is dependent on rate of hydrolysis and condensation. The two process are explained by taking the example of alkoxysilane conjugated acid.

1. **Hydrolysis** $\qquad$ $Si - OR + H_2O \rightarrow Si - OH + ROH$

2. a) **Homocondensation** $\quad$ $Si - OH + Si - OH \rightarrow Si - O - Si + H_2O$

$\quad$ b) **Heterocondensation** $\quad$ $Si - OH + Si - OR \rightarrow Si - O - Si + ROH$

$\quad$ a) **Olation**

Olation is the formation of hydroxyl bridges between adjacent metal centers occur via H_3O_2 intermediates. Nucleophilic substitution of hydroxyl groups occur for coordinately saturated metals and limited to acidic conditions. Rate of olation is dependent on metals electronegativity, electronic configuration and size. Rate of olation is greater if charge density is lower. If hydrolysis rate is faster sol-gel is less branched and resulting gel is microporous.

Figure 3.2- a condensation reaction in which hydroxo bridges are formed and water is eliminated [187].

b) Oxolation

Oxolation is a condensation reaction in which oxo-bridges are formed. It is favored for coordinatively unsaturated metal centers but also possible for saturated metal centers. The nucleophilic substitution results in face or edge shared polyhedral. Oxolation can be carried out over wide range of pH. At isoelectric point oxolation is minimized. Oxolation is a two-step process with never diffusion limited and slow kinetic rate. Sol-gel is highly branched and resulting gel is mesoporous when condensation rate is fast.

Figure 3.3- two step mechanism results in formation of oxo bridges [187].

Condensation is followed by polymerization also known as type of inorganic polymerization. A rigid gel is formed when polymeric cross-linking becomes extensive. Porosity of gel strongly depends on cross-linking.

3.1.2 Texture of solid obtained from sol-gel

The texture of solid obtain sol-gel process is generally powder after drying characterized by several macroscopic quantities. Theses macroscopic quantities are:

1. Specific surface area i.e., total internal external surface m^2g^{-1}.
2. Porosity i.e., total porous volume, pore size and distribution.
3. Density i.e., size and dispersion of particles.
4. Hydrophilicity i.e., capacity of materials to absorb water.

Different materials have different texture depending on the experimental conditions. From chemical reaction to drying every step have great influence on texture. For the production of stable and reproducible material precise experimental conditions and sufficient aging time give the successful results. Texture of material greatly influences its different properties e.g., for a high quality ceramic monodisperse repartition is obligatory.

Heterogeneous catalyst properties are intensely depended to interaction between surface of support and catalyst. Theses catalyst has OH groups at the surface tightly bounded to metal as ligand but access to free electrons is allowed. The number and distribution of these OH groups are fundamental to efficiency of heterocatalyst.

3.2 Materials and Method

3.2.1 Materials

All chemicals purchased from: titanium tetrachloride ($TiCl_4$), (BDH), ammonia (NH_3), (RDH), ethanol (C_2H_6O), (Sigma Aldrich), zinc nitrate ($Zn(NO_3)_2.6H_2O$), (BDH), silver nitrate ($AgNO_3$) (BDH), Eosin Y ($C_{20}H_6Br_4Na_2O_5$) (BDH), Methyl orange ($C_{14}H_{14}N_3NaNO_3S$) (BDH) and used without further purification.

3.2.2 Methods

3.2.2.1 Synthesis of bare and doped TiO_2 photocatalyst

All chemicals purchased from: titanium tetrachloride ($TiCl_4$), (BDH), ammonia (NH_3), (RDH), ethanol (C_2H_6O), (Sigma Aldrich), zinc nitrate ($Zn(NO_3)2.6H2O$), (BDH), silver nitrate ($AgNO_3$) (BDH) and used without further purification.

TiO_2 nanoparticles have been synthesized by a simple, cheap, and reproducible wet chemical sol-gel process. Titanium tetrachloride ($TiCl_4$) has been used as precursor. An appropriate amount of $TiCl_4$ has been added to the mixed solvent of ethanol and deionized water (7:10). The solution was left for stirring for sometime within an ice bath. The ammonia solution was added to above solution under constant stirring. This resulted into the white colored solution. After 1h stirring, the solution was left for gelation for a day. The gel was washed several times using de-ionized water. The gel was collected and dried in air at 80^oC overnight, followed by annealing in 400^oC for 3h. The annealed sample has been grinded using mortar and pestle. In order to prepare the Zn/Ag doped TiO_2 samples same procedure has been followed with 1%, 3% and 5% Zn/Ag dopants. For doping we have used $AgNO_3$ and $Zn(NO_3)_2.6H_2O$ for Ag and Zn sources respectively.

3.3 Photocatalytic degradation procedure

Heterogeneous photocatalysis is one of new techniques for the removal of wastes form water using nanoparticles most commonly TiO_2 nanoparticles. In this research photocatalytic efficiency of undoped and doped TiO_2 nanoparticles have been studied by using two commonly used industrial dyes eosin y and methyl orange. Their chemical structures are shown below:
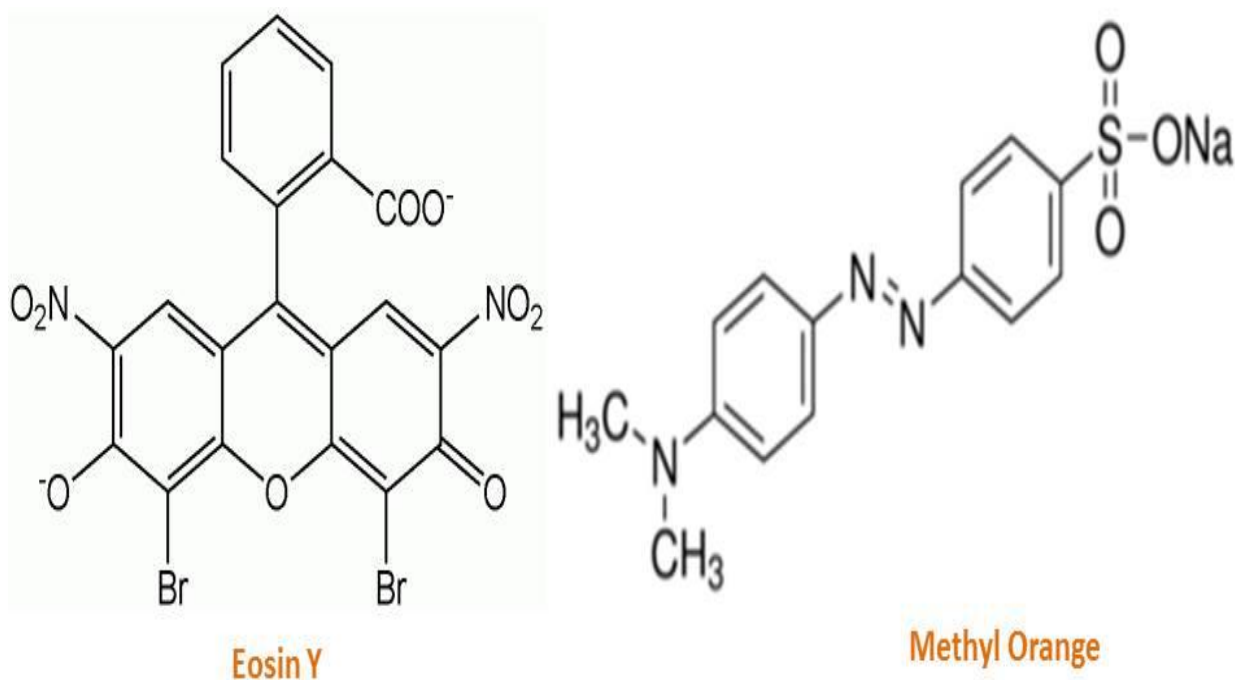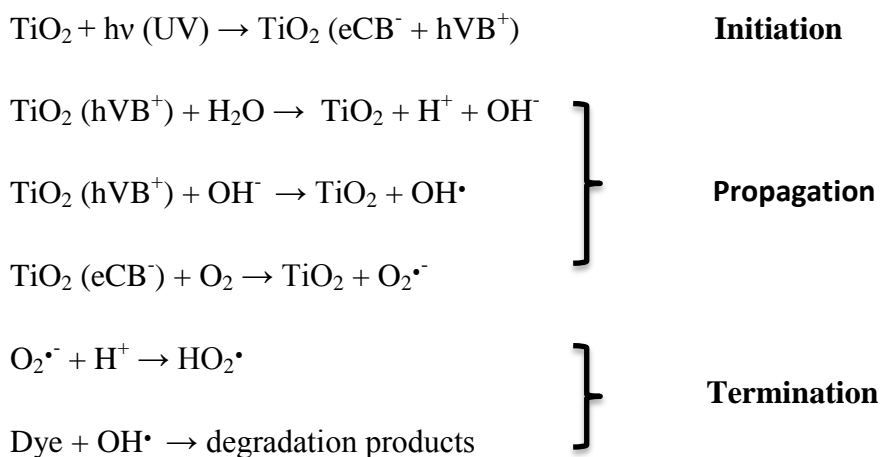
Figure 3.4- Eosin Y and Methyl Orange structure

The superoxide anion $O_2^{\bullet-}$ and $OH^{\bullet}$ radicle are together responsible for heterogeneous TiO_2 photodecomposition of organic waste. The whole mechanism is elaborated below:

$TiO_2 + h\nu\ (UV) \rightarrow TiO_2\ (eCB^- + hVB^+)$ **Initiation**

$TiO_2\ (hVB^+) + H_2O \rightarrow\ TiO_2 + H^+ + OH^-$

$TiO_2\ (hVB^+) + OH^- \rightarrow TiO_2 + OH^{\bullet}$ **Propagation**

$TiO_2\ (eCB^-) + O_2 \rightarrow TiO_2 + O_2^{\bullet-}$

$O_2^{\bullet-} + H^+ \rightarrow HO_2^{\bullet}$

$Dye + OH^{\bullet} \rightarrow$ degradation products   **Termination**

Dyes have colored solution and characteristics wavelength value known as λ_{max} in visible region. At that particular wavelength dyes have maximum absorbance and all photodegradation measurements are taken at that value. λ_{max} can be calculated using UV/Vis spectrophotometer. Eosin Y and methyl orange have λ_{max} at 515nm and 465nm. By changing pH value of the dye color changes and hence λ_{max}, also pH effects the degradation rate of dye.

3.3.1 Calibration curve

Generally in chromatography different analytes have different response to detectors. Similarly the analyte with different concentrations have different detectors response. The analytical analysis has been done for known quantities or concentrations to interpret the response of unknown analyte. For this we draw a calibration curve between absorbance (a.u) and concentration (mg/L) using UV/Vis spectrophotometer. In our case the analyte are dyes. The different solutions prepared of known concentration of dyes are known as standard solutions. Then a best straight line is drawn between the linear portions of the spectrophotometer data. By using equation of straight line slop and intercept is figure out. The equation of straight line is given as:

$$y = mx + c$$

Here

y = absorbance m = slop x = concentration c = y-intercept

By drawing trend line regression coefficient or coefficient of determination (R^2) is calculated which determine how perfectly data fits into straight line. Its value must be nearly or equal to 1. Regression value 1 states that data is perfectly fitted to straight line. Whereas if value is 0 it indicates data is not well fitted to straight line.

The calibration curves have been drawn for eosin y and methyl orange are shown in fig. 3.5. The absorbance has calculated for known concentrations of both dyes 0-30 mg/L. The obtained data best fits to straight line with regression coefficient values nearly 1. Calibration curve has drawn between the obtained absorbance values from spectrophotometer and known concentration values. The regression coefficient for eosin y and methyl orange is 0.999 and 0.9995 respectively, which shows that all data is linearly fitted to straight line.
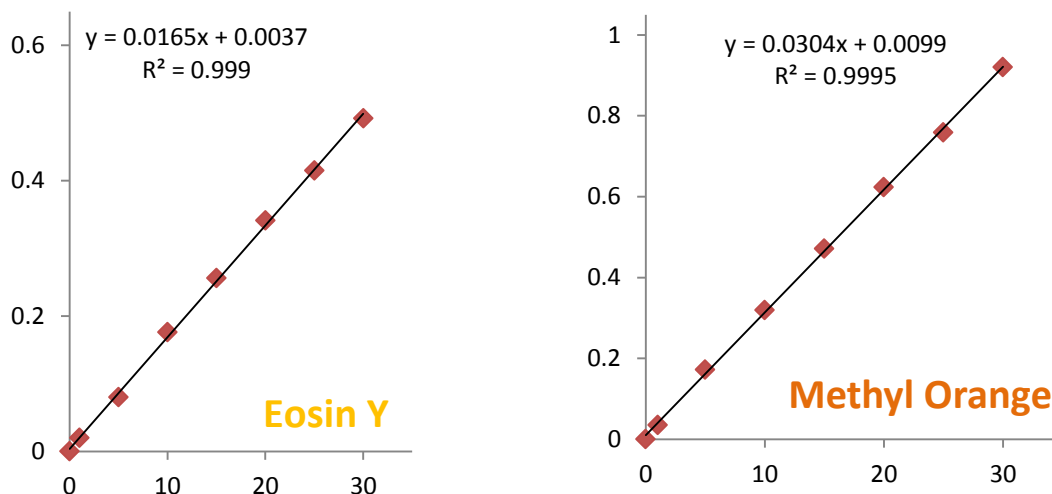
Figure 3.5- calibration curves for Eosin Y and Methyl orange

All reactions were performed in a photocatalytic chamber equipped with 90watt UV-B lamps having wavelength range 280-315 nm and ice was placed inside in order to maintain the temperature between 25-30°C. The whole chamber was laminated by aluminum foil in order to keep the UV radiations inside.

3.3.2 Solution preparation

Stock solution of 1000mg/L was prepared for each dye in volumetric flask and then concentration was downed up to 5ppm. Different experiments were performed in order to set the optimum value of photocatalyst for degradation of 5ppm of dye. It was observed that in my experiment 300mg/L and 500g/L of catalyst is suitable for 5ppm eosin y and methyl orange degradation in 1h respectively. The pH of both dyes was adjusted at 3.

The total volume of 5ppm solution was 100ml. All measuring conditions for both dyes were same. Initially catalyst was added to dye solution and stir in dark for 30min to develop adsorption-desorption equilibrium then exposed to UV lamp. The solution was constantly stirred at 300rpm to keep the catalyst in suspension. The 5ml sample was ejected before exposure to UV lamp then ejected after every 20min to calculate absorbance in periodic manner. The distance between solution and lamps was almost 20cm.

3.3.3 Degradation percent calculation

The degradation percent was calculated using:

$$\% \; degrataion = \frac{A_o - A_t}{A_t} \times 100$$

A_o = Initial absorbance A_t = absorbance at time t

3.3.4 Concentration calculation

Concentration of the dye was calculated by using Beer-Lambert law given as:

$$A = \in cl$$

Where

A = absorbance at particular wavelength.

$\in$ = molar absorptivity or molar extinction coefficient (L/mol cm).

c = concentration of the sample in moles per liter (mol/L) of the solution.

l = path length of the sample solution in centimeters (cm).

3.3.5 Reaction kinetics and rate of reaction

One of the most empirical calculations we need for any chemical reaction to be studied for is how concentration of reactants and products alter with time. Generally a reaction proceeding truly when concentration of reactants decreases and products increases with respect to time. Intermediates formed during reaction but their concentration decreases with time.

Rate of reaction is defined in terms of change in concentration of reactants and products with time. The rate of change in any specie is proportional to slop of concentration curve. The order of reaction is determine by sum of power n i.e. n = 0, 1, 2... and order of reaction is defined by particular specie in the reaction as the power to which its concentration is raised. The rate constant k has units of time^{-1} concentration^{-1}. The rate law varies with different order of reaction. Generally chemical reactions are of:

1. **Zero-order reaction**

The zero-order reaction is independent of participating substance or reactants n = 0. The reaction may be zero-order in concentration ranges, in low concentration range it does not hold. The rate of reaction is determined by certain limiting factors like for a catalytic reaction it depends on rate of availability of surface sites and diffusion of reactants.

2. First-order reaction

The first order reaction has order of reaction n = 1. As it depends only on concentration of one reactant that forms products. Radioactive decay processes are example of first order reactions as they involve only specie in the entire reaction and nucleophilic substitutions give products. The rate constant is calculated by slop of concentration curve.

3. Second-order reaction/Pseudo first order reaction

In second-order reactions generally two reactants are involved to form products have order of reaction n = 2. Second order reaction is also known as Pseudo first order in some cases when one of the reactant concentrations remains unchanged during entire reaction. So experimental conditions show the reaction is first order. Although we have two reactants but rate of reaction depends only on one specie. Catalytic reactions are generally explained on the basis of Pseudo first order as it involves two reactants but concentration of catalyst remains unchanged during entire reaction. The slop or reaction constant k is calculated by using following equation.

$$ln(\frac{C_o}{C_t}) = kt$$

Where

C_o = Initial concentration (mol/L)　　　　C_t = concentration at time t (mol/L)

t = time (min)　　　　k = rate constant ($t^{-1}con^{-1}$)

Chapter 4

Characterization Techniques

The following characterization techniques have been used to study the as synthesized photocatalysts.

1. X-ray diffraction to study the crystallographic structure.
2. Scanning electron microscope was used to study surface morphology.
3. Fourier transformation infrared spectroscopy.
4. UV-Vis spectrophotometer (PG Instrument T90) for bandgap analysis and dye degradation study.

4.1 X-ray diffraction (XRD)

X-rays are electromagnetic radiations with very short wavelength. They were discovered in 1895 by Roentgen, a German physicist. They were named so because at the time of discovery their properties were unknown. In 1912, exact nature of x-rays was discovered along with phenomena of x-ray diffraction by crystal. X-ray diffraction was new technique to investigate crystallinity of any material at atomic level. The wavelength range of x-ray diffraction is in range of 0.5-2.5 Å which is about same size as atom. In electromagnetic spectra x-rays lie between ultra violet and gamma rays.

XRD is one of the most commanding scientific tools to identify and quantify a number of materials [188, 189]. The concentrations or absolute amount of mixtures having same chemical properties but different crystal structures can be analyzed by using this technique [190]. A nondestructive technique determines the crystalline phase of any material along the properties of these phases, arrangements of atoms and thin film thickness. Every material has its own distinctive XRD pattern which gives its proof of identity. Crystallography, after the identification of material by XRD determines various properties crystal like packing fraction, interatomic distances, angles etc. XRD make available feature statistics of following aspects:

1. The pattern of peaks their position and integrated intensities obtained by XRD is compared to known database to calculate presence and absence of particular phase.

2. The indistinguishable phases in solution i.e., some or all phases are identical chemically can be analyzed "quantitative phase analysis". By XRD mixture of more than two phases can accurately be analyzed by means of phase fraction.

3. By comparing old and new structure an unknown material crystallinity can be calculated. Also spacing between rows of atoms known as d-spacing is calculated.

4. XRD patterns as a function of temperature, time and pressure can probe the phase reactions and solid state reaction.

5. Elusive structure details like lattice vacancies can be extracted by using high sample quality and high resolution data.

6. The crystal structure of completely unknown material can be calculated even no previous data is available except stoichiometry but it needs high resolution data and interpretation.

For XRD, typical uniform sample is required for analysis and measurement but in case of mixture the concentration ratio needs to be same for all points in the mixture sample. For thin films and powders real samples are not uniform and data is collected in the form of map instead of signal [190]. By advances in micro and nano beam optics have brought opportunity to extend XRD for complete 2D and inhomogeneous mixture analysis but it still require XY scan [191]. XRD analysis, full width half maxima (FWHM) morphology index (MI) is derived; which gives interrelationship between surface area (inverse) and particle size (direct).

4.1.1 Bragg's law

W.H Bragg and W.L Bragg in 1913, develops a relation why cleavage faces of crystal appears to reflect incident beam at certain angle θ. Bragg's law identifies the angle at which diffraction peaks occur for incident radiation. Bragg's derived condition for constructive interference. Diffraction of x-rays occurs when reflections occur constructively without loss of energy and are inphase. So diffraction pattern is based on scattering followed by interference.

Bragg's law defines constructive interference occurs only when path difference is integral multiple of wavelength i.e.

$$2dsin\theta = n\lambda$$

Here

λ= wavelength   n= order of diffractiond= d-spacing between two adjacent planes

θ= angle of incidence/scattering

Bragg's diffraction only occurs when:

$$n\lambda \leq 2d$$

No diffraction occurs when above condition is not satisfied. That's why visible light can't be used for crystallographic study.

4.1.2 Debye-Scherer formula

The average particle can be calculated by using Debye-Scherer formula:

$$D = \frac{0.9\lambda}{\beta Cos\theta}$$

Here

D= particle diameter   λ= wavelength of x-ray   θ= diffraction angle

When particle size is less than 100nm an appreciable boarding in XRD pattern occurs due to particle size and strain. Average size of particle is calculated by total line broadening observed.

4.2 Scanning electron microscopy (SEM)

SEM is most frequently used characterizing tool now-a-days because of its huge deepness of focus, large magnification, easy sample observation and high resolution. Topography, morphology, crystallography, chemistry and orientation of grains in nanostructured materials can make known via this revolutionary technique. Its depth of focus is 500 times better than optical microscope. An electron beam is accelerated towards the specimen with voltage approximately 20kV. By increasing voltage interaction area increases but decreased by increasing atomic number. Electron beam scatter both elastically and in-elastically giving rise to number of signals as shown in figure:
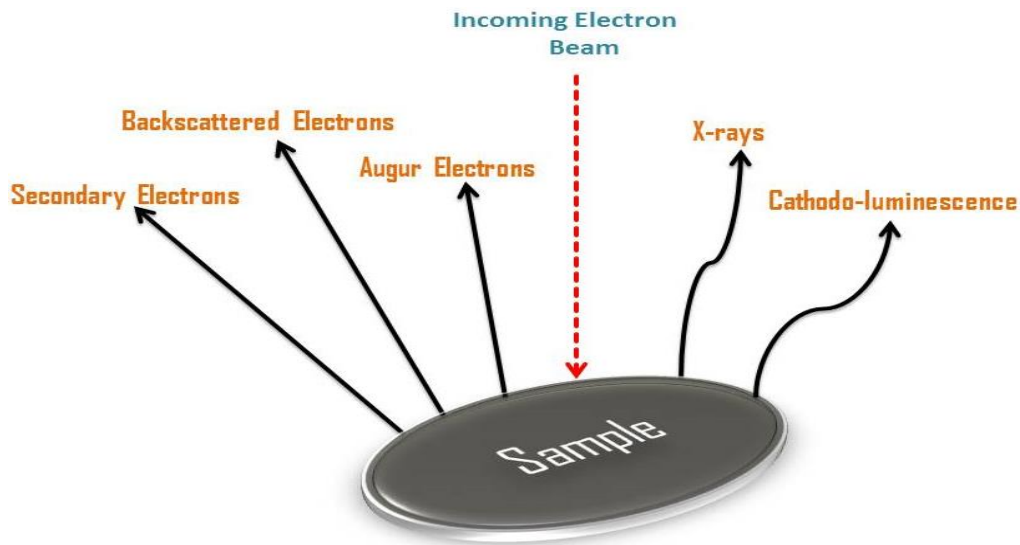
Figure 4.1- Scattering of electron beam after interaction with specimen

The signals emitted in the form of photons or electrons are collected on cathode ray tube screen in the form of image. Three types of images can be displayed on cathode ray tube.

I. Secondary electrons (SE) image

SEs give topographical information. They are loosely bounded electrons and scatter inelasticaly by incoming atomic electrons. SEs has energy less than 50keV. SEs are of two types SE 1 and SE 2 can be differentiated as:

SE 1 are those that are generated when electron beam hit the surface of specimen producing high resolution image only limited by electron beam diameter. When backscattered electrons after several elastic collisions returned to surface they kick out some surface electrons known as SE2. SE2 has poor resolution as compared to SE1. Everhart-Thornley detectors are used to detect SEs.

Factors effecting SE emission

1. Local curvature of the surface
2. Atomic number
3. Beam and beam current
4. Work function of the surface

II. Backscattered electrons (BSEs)

When electron beam is directed towards the sample some electrons due to strong electromagnetic field of nucleus are retarded and if scattering angle is greater than 180° they

escape towards the detector known as BSEs. They are high energy electrons and scatter elastically. BSEs can be of type 1 or type 2 but most BSEs are BSE2 type. Solid state detectors are used for BSEs.

Factors effecting BSE emission

1. Average atomic number
2. Direction of irradiation surface

III. X-ray elemental map

As electrons excite and de-excite number of photons also generate inside the SEM chamber giving X-ray elemental map also known as energy-dispersive spectrometer (EDS). But they have poor resolution as compare to SEs and BSEs and very few in numbers so needs long signal collection time. It can be used by several approaches including line scan, spot examination, chemical concentration plot.

4.2.1 Components of SEM Instrument

Basic components of SEM are shown in fig. 4.2 below:
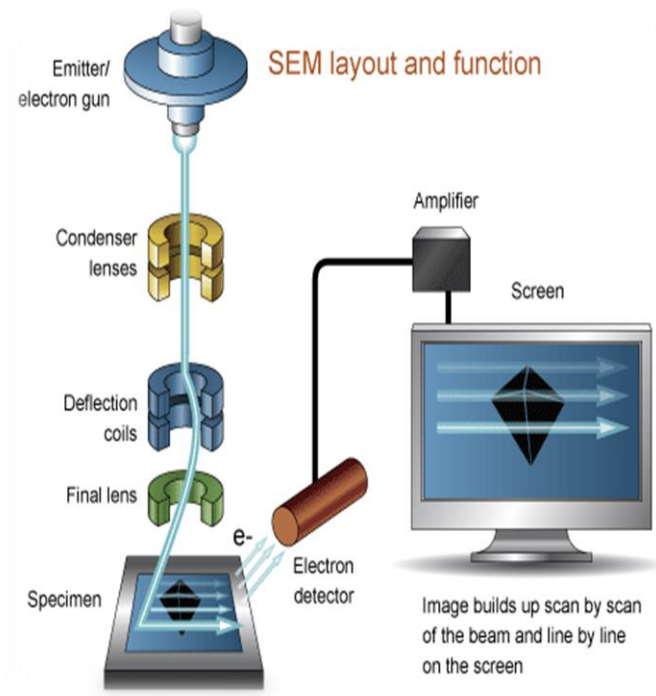
Figure 4.2- Basic instrumentation of SEM

4.2.2 Operating conditions for SEM

- Vacuum is necessary inside the chamber because thermal stability is necessary for filament functionality and signals travels directly towards sample.
- Only solid sample is detectable, in case of liquid sample it is vaporized before detection.
- Any type of samples are coated with conducting metals such as gold before irradiation of electrons.

4.2.3 Resolution and Magnification in SEM image

Resolution strongly depends on sampling volume from which signals originates. Image seems in focus only if sampling volume is smaller than picture element and features can be resolved. For high magnifications, the sampling volume signal density is not uniform hence real signal distribution across the sampling volume becomes critical. Magnification is the function of scan length and given as:

$$M = \frac{L}{l}$$

The scan is reproduced on cathode ray tube versus distance and width in time. It is independent of lens used and can be changed with respect to area by holding constant film dimension. Magnification is inversely proportional to scanned area. Magnification is the strength of SEM image quality and altered within complete range without loss of image quality. Characteristic magnification varies from 10X-100,000X.

4.2.4 Advantages of SEM

- Images of SEM have high resolution, magnification and depth of focus.
- SEM is able to determine crystalline phase of any material.
- It is a non-destructive technique and sample can be analyzed further after SEM even EDS analysis no sample loss occur.

4.2.5 Limitations of SEM

- Vacuum compatibility is vital.
- Size restriction.

4.3 Fourier-transform infrared spectroscopy (FTIR)

Due to several limitations in dispersive infrared spectrophotometer including wavelength inaccuracies, slow monitoring process, light loss due to narrowness of focusing slit and thus poor sensitivity has led to the development of FTIR.

FTIR is a single beam instrument overcoming all drawbacks associated with dispersive instrument. The basic principle of FTIR is based on interferometer resulting in interferogram and resultant frequency spectrum is processed and analyzed by a wel-known mathematical tool known as Fourier transformation. FTIR is a basic tool to analyze the functional groups, type of bonds and impurity in sample. The IR region is further into three sub regions known as:

- Far-IR (400-20) cm^{-1},
- Mid-IR (4000-400) cm^{-1}
- Near-IR (14000-4000) cm^{-1}.

4.3.1 The Interferometer

The interferometer is an optical device which measures all infrared frequencies simultaneously. A unique type of signal is produced by interferometer known as interferogram, encoded with all infrared frequencies.

An interferometer consists of three basic parts fixed mirror, moveable mirror and beam splitter. Beam splitter is a semi-silvered mirror or germanium (Ge) thin film sandwiched between two potassium bromide (KBr) plates. It reflects and transmits the beam equally towards mirror. Both mirrors are at right angle to each other as shown in fig below:
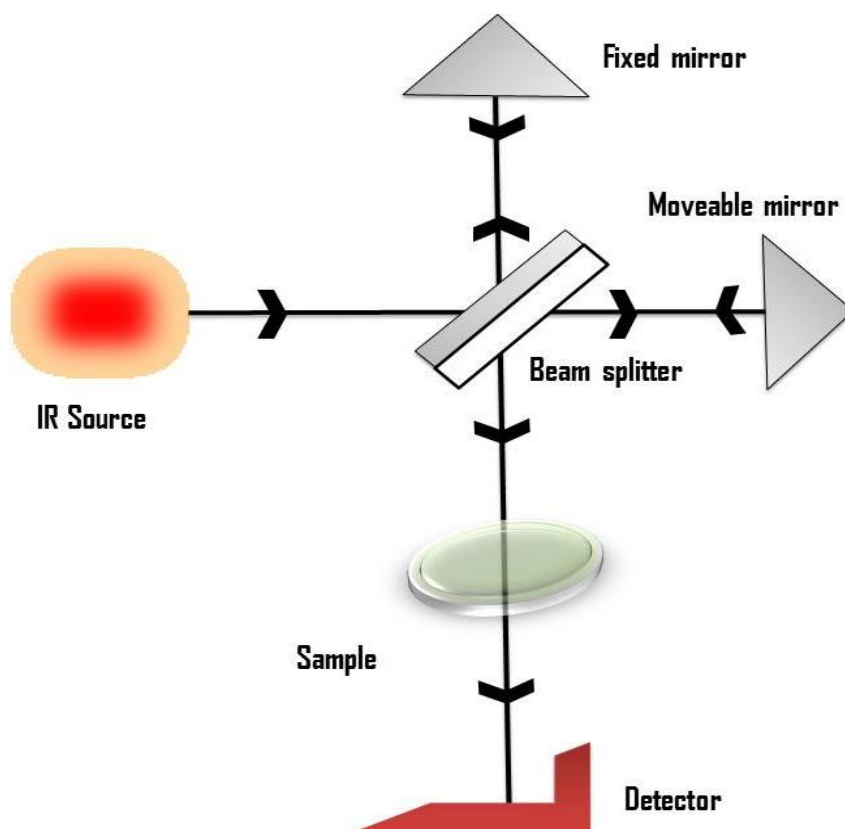
Figure 4.3- Optical diagram of Michelson's Interferometer

Light received from the IR source is splitted by beam splitter such that reflected and transmitted towards fixed mirror and moveable mirror respectively. Both beams reflect back and recombine at beam splitter. This signal is known as interferogram. Interferogram is again splited and one half goes towards sample followed by detector and other half moves back to source. This signal is collected very quickly in one second thus time is reduced to seconds. The sample is in the form of KBr pellets.

The detector must be sensitive and photometrical accurate such that it contests the speed of instrument. Pyroelectric material based detectors are most common. These signals are analyzed by computer decoded Fourier transformation tool which gives desired spectral information.

4.3.2 Advantages of FTIR

Few major advantages of FTIR over dispersive IR are:

- All frequencies can be measured simultaneously within seconds instead of minutes also known as felgett advantage.

- Sensitivity and optical through put of FTIR is much high which results in fast scan and reduced noise. As no slit is used so all radiant energy is utilized which enhances sensitivity.

- The moving mirror is only moving part of the instrument which reduces the mechanical breakdown.

- The instrument has high resolution up to $0.1 cm^{-1}$.

- The instrument consists of Helium-Neon laser as slandered calibration so user calibration is not needed.

4.5 Ultraviolet/Visible spectroscopy (UV/Vis)

In UV (10-400 nm) / Vis (400-800 nm) the absorption of radiations by organic or inorganic molecules is based on the same principle and hence results in alike molecular excitation therefore they are scrutinized concurrently as UV/Vis spectroscopy. It is also known as electronic spectroscopy as absorption of UV/Vis results in transition between electronic energy levels. Conventional UV/Vis spectrophotometer is not able to scan the region below 200nm as in this region oxygen in the air absorbs strongly, hence it is known as vacuum region. The instrument for vacuum region is quite expensive and usually not essential for revelation of molecular structure.

4.5.1 Basic principle of UV/Vis spectroscopy

The basic mechanism of UV/Vis spectroscopy is based on absorption of source radiations and molecules electronic transitions. The electrons excite when molecules absorb UV/Vis radiations. The wavelength of radiation depends on the energy difference of two different states. It is therefore assumed that only one electron is excited by absorbing only one photon while others remain unaffected. This is because molecule absorbs UV/Vis of particular wavelength.

The electronic transitions based on Franck- Condon principle i.e., vibrating atoms of the molecule don't change their position because electronic transitions occur so expeditiously. The four types of electronic transitions are associated with UV/Vis absorption i.e.,

1) $\sigma \rightarrow \sigma^*$ (saturated hydrocarbons)
2) $n \rightarrow \sigma^*$ (saturated molecules containing hetero-atoms)
3) $\pi \rightarrow \pi^*$ (conjugated systems)

4) n → π* (hetero-atoms containing double or triple bonds)

Position and intensity are two key characteristic to absorption. Intensity at particular wavelength depends on number of molecules that absorbs the radiation of that particular wavelength. The intensity of absorption is conveyed as molar absorptivity (ϵ) and can be measured either as absorbance (A) or transmittance (T). Both are expressed as:

$$A = \log(^{I}/_{I_o}) \quad \text{Or} \quad A = log\, ^{1}/_{T}$$

$$T = \,^{I}/_{I_o}$$

Where

I_o = incident radiation intensity   and I = transmitted radiation intensity

The range of commonly calculated absorbance is 0-2.

4.5.2 Beer-Lambert law

Beer-Lambert law states that absorbance is proportional to concentration and path length traveled by UV/Vis radiation in a sample.

$$A \propto cl$$

$$A = \epsilon\, cl$$

Where

A = absorbance at particular wavelength.

ϵ = molar absorptivity or molar extinction coefficient (L/mol cm), constant for solute at particular wavelength. It calculates how much light is absorbed by solute at particular wavelength.

c = concentration of the sample in moles per liter (mol/L) of the solution.

l = path length of the sample solution in centimeters (cm).

When solution is concentrated the solute molecules get closer to each other and influence their properties including ϵ. So at very high concentrations solute act as solvent and

absorbance alter. Thus beer's law fails and don't hold for solutes having absorbance greater than 1.

4.5.3 Instrumentation

For measurement of absorbance both single and double beam instruments are used. The essential are in shown in fig. 4.4 below:
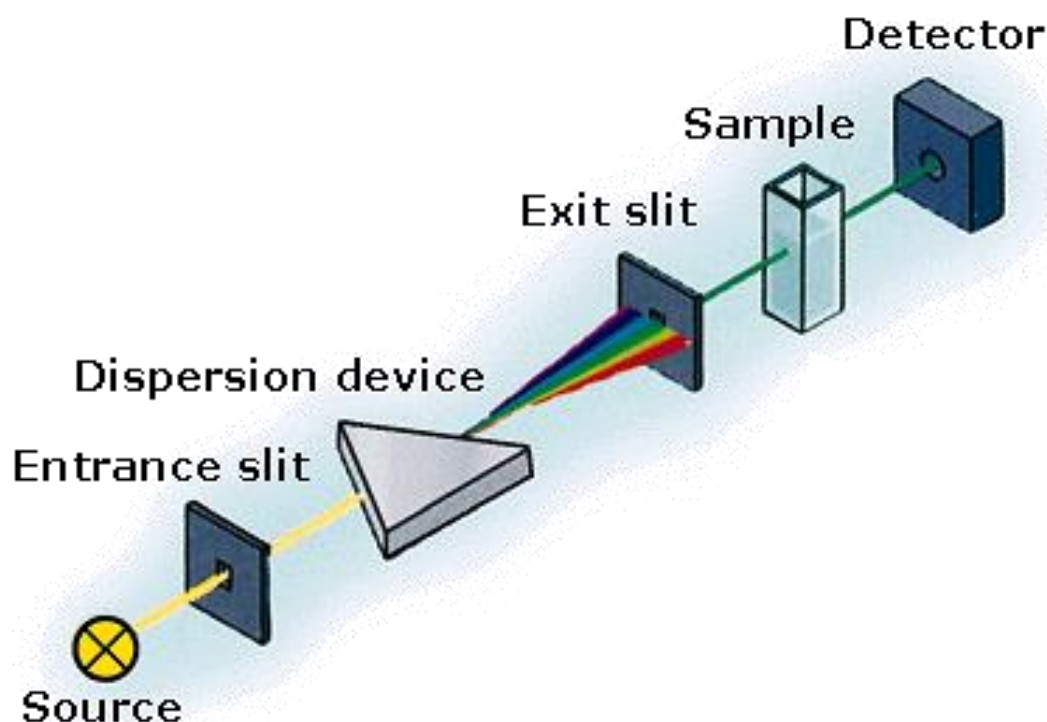
Figure 4.4- Components of UV/Vis spectrophotometer

A double beam instrument divides the incident radiation beam into two equal parts which then passed through two different cells. Cells contain reference solvent and sample solution respectively. Source of radiation for UV and visible ranges are hydrogen or deuterium lamp and tungsten filament respectively. A monochromator consists of prism or diffraction grating. Grating disperses the polychromatic radiation into monochromatic bands. Cell or cuvette containing sample is of quartz and walls must be cleaned before use. The glass cuvette can't be used in case of UV radiation because glass absorbs UV radiation. Cuvette length ranges from 0.1cm-10cm.

The optical chopper rotates at the frequency of 10cps and directs the reference and sample alternatively to the detector. Chopper is used in double beam instruments. A detector

must be sensitive, having low signal to noise ratio and stable to desired wavelength. Most commonly used detectors are photomultiplier and phototubes.

4.5.4 Solvents for UV/Vis spectroscopy

The solvent used for analysis must be transparent within desired wavelength range and inert to solute. Like UV/Vis spectra of aldehydes can't be examined in alcohols as a solvent. Most commonly used solvents are water, ethanol and n-hexane.

Table 4.1- Solvents for UV/Vis spectroscopy

Sr. No.	Solvents	Wavelength (nm)
1	Water	190
2	Ethanol	210
3	Cyclohexane	210
4	n-hexane	200
5	Methanol	210
6	Carbon tetrachloride	260
7	1,4-Dioxane	220
8	Tetrahydrofuran	220
9	Chloroform	240
10	Acetonitrile	190

4.5.5 Regions of visible spectrum

A white light consists of all color and color appears to human eye when specific wavelength is absorbed from white light by a substance e.g., when a substance absorb blue light it reflects yellow radiation an d hence a substance appears yellow. The visible region of electromagnetic spectra is divided into further sub regions which show the relationship between electronic transition and color.

Table 4.2- Regions of visible spectrum

Region	Wavelength (nm)	Color
Red	800-650	Green-Blue
Orange	650-595	Blue-Green
Yellow	595-580	Blue
Yellow-Green	580-560	Violet
Green	560-500	Purple
Blue-Green	500-490	Red
Green-Blue	490-480	Orange
Blue	480-435	Yellow
Violet	435-400	Yellow-Green

Chapter 5

Results and Discussion

5.1 XRD analysis

To study the crystal structure and phase composition of prepared catalysts the XRD (Theta-theta, Stoe Germany) analysis has been done. The XRD analysis has also been used to confirm the doping of Ag, Zn and co-doping of Zn/Ag into the TiO_2 host matrix. The XRD pattern has been recorded in the angle range of 20°-70°.

The XRD results of Zn doped TiO_2 have been shown in the Fig. 5.1. The peaks at 25.06^o, 37.6^o, 37.9^o, 47.8^o, 53.77^o, 54.77^o, 62.6^o and 68.4^o are assigned to (101), (103), (004), (200),(105), (211), (213), and (116) planes of anatase phase of TiO_2. In Zn doped samples it can be observed that all the three 1, 3 and 5 mol% have shown all of the above mentioned peaks, thus presenting Zn^{2+} cations have been successfully doped into the host matrix without altering the crystalline structure and phase of TiO_2. The results obtained from XRD match well with the previous reports [168] and JCPDS card number 00-001-0562. Moreover there is a shift in main peak (101) due the difference in atomic radii of Ti^{4+} and Zn^{2+} cations. Because of small ionic radii of Zn^{2+} cation it is easily substituted into host matrix and no phase transformation occur.
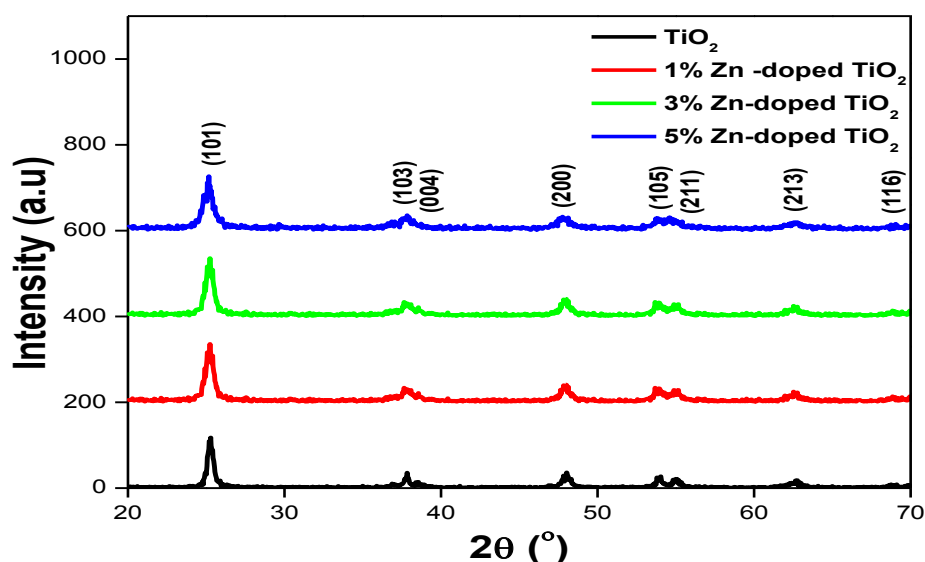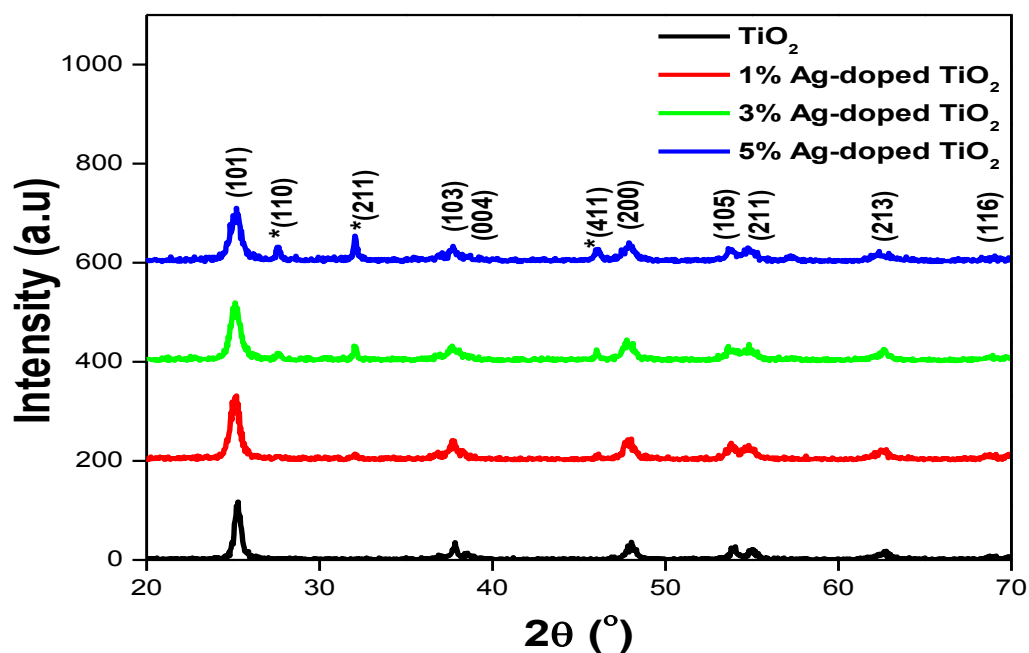

Figure 5.1-The XRD analysis of TiO_2 and 1, 3, 5 mol% Zn doped TiO_2 nanoparticles

The XRD results of Ag doped TiO_2 have been shown in the Fig. 5.2. The peaks at 25.06^o,37.6^o, 37.9^o, 47.8^o, 53.77^o, 54.77^o, 62.6^o and 68.4^o can be assigned to (101), (103), (004), (200),(105), (211), (213), and (116) plane of anatase phase of TiO_2. In Ag doped samples it can be observed that 1, 3 and 5 mol% have shown successfully Ag doping into the TiO_2 host matrix, without altering the crystalline structure of TiO_2. But in 3 and 5 mol% along with above mentioned diffraction peaks phase transformation occurs as peaks appearing at 27.2^o, 32.3^o and 46.4^o can be assigned to (110), (211) and (411) of the rutile phase of TiO_2. This shows that Ag^{1+} cation have induced the phase transformation of TiO_2 when doping concentration of Ag is increased. The results obtained match well with the obtained results [192] and JCPDS cards 00-001-0562 and 00-002-0494. As anatase is metastable phase of TiO_2 and ionic radii of Ag^{1+} cation (1.26 Å) is large as compared to Ti^{4+} cation (0.75 Å) so Ag1+ cations don't incorporate completely into host matrix resulting in phase transformation.

Figure 5.2- The XRD analysis of TiO_2 and 1, 3, 5 mol% Ag doped TiO_2 nanoparticles

The XRD results of Zn/Ag co-doped TiO_2 have been shown in the Fig. 5.3. The peaks at 25.06^o,37.6^o, 37.9^o, 47.8^o, 53.77^o, 54.77^o, 62.6^o and 68.4^o can be assigned to (101), (103), (004), (200),(105), (211), (213), and (116) plane of anatase phase of TiO_2. In Zn/Ag co-doped samples it can be observed that all the three 1 mol%, 3 mol%, 5 mol% have shown all of the above mentioned peaks, thus presenting Zn and Ag ions have been successfully doped into the TiO_2 host matrix, without altering the crystalline structure of TiO_2. A very low intensity at 27.1^o with (110) plane is observed which is due to the presence of rutile phase in the prepared samples i.e., Ag has induced phase transformation from pure anatase to rutile. The

52

results obtained from XRD match well with the previous reports [182] and JCPDS card number 00-001-0562. In co-doped samples the shift in main peak indicates that Ti^{4+} cations are successfully replaced by Zn^{2+} and Ag^{1+}. Moreover Zn^{2+} resists the phase transformation of TiO_2 and there is only a bit of transformation in 5 mol% co-doped sample because of Ag^{1+} cations.
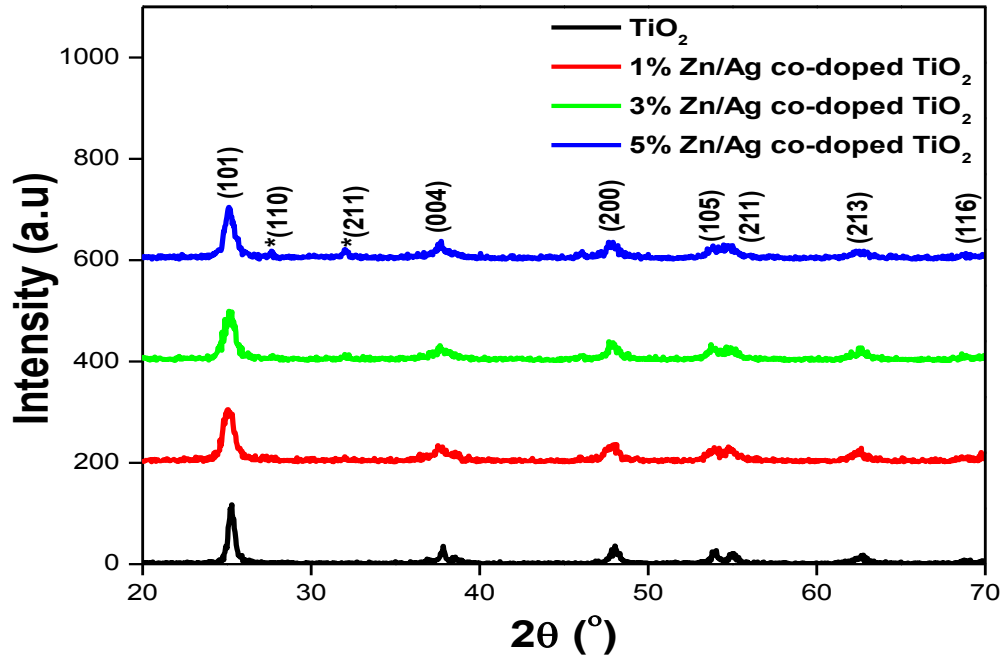
Figure 5.3- The XRD analysis of TiO_2 and 1, 3, 5 mol% Zn/Ag co- doped TiO_2 nanoparticles

5.1.1 Crystal size calculation

The high intensity of XRD peaks shows that as synthesized particles are highly crystalline and broadness of each peak reflects the small crystallite size. The crystal size has been calculated by using Debye-Scherer formula:

$$D = \frac{k\lambda}{\beta Cos\theta}$$

$$k\lambda = 0.1386$$

The average crystallite size was calculated form anatase (101) diffraction peak broadening which represents 100% anatase. The little shift in peak position is due to difference in ionic radii of Ag, Zn and Ti. The crystallite size of TiO_2 nanoparticles is calculated as 29nm and reduced up to 12nm by doping. The total boundary energy of TiO_2 increases when grain size decreases. The calculated crystal size is presented in table 5.1 below:

Table 5.1- Crystal size of as prepared TiO_2 and doped TiO_2

Sample	2θ (^{o})	θ (^{o})	FWHM β (Radians)	Cosθ	βCosθ	Size (nm)
TiO_2	25.24	12.62	0.004887	0.97584	0.004769	29
1 mol% Zn doped	25.24	12.62	0.010996	0.97584	0.01073	13
3 mol% Zn doped	25.15	12.58	0.006807	0.97599	0.006644	21
5 mol% Zn doped	25.21	12.6	0.010996	0.97591	0.010731	13
1 mol% Ag doped	25.2	12.61	0.009599	0.97588	0.009367	15
3 mol% Ag doped	25.09	12.55	0.010996	0.97611	0.010733	13
5 mol% Ag doped	25.25	12.63	0.012392	0.9758	0.012092	12
1 mol% Zn/Ag co- doped	24.94	12.47	0.012392	0.97641	0.012099	12
3 mol% Zn/Ag co- doped	25.33	12.67	0.010996	0.97564	0.010728	13
5 mol% Zn/Ag co- doped	25.12	12.56	0.008203	0.97607	0.008007	17

5.2 Scanning electron microscopy (SEM)

SEM model number JSM-6490A analytical SEM JEOL Japan along with JSC-1500 ion sputtering device (automatic gold coater) has been used to investigate the particles morphology and size. The morphology and particle size calculated for each sample is in desired range and can be used for potential applications. The particle sizes and morphology are given in table below:

Table 5.2- Particles sizes and morphology

Sample	Average Particle size (nm)	Morphology
TiO$_2$	36nm	Spherical
1 mol% Zn doped	21nm	Spherical
3 mol% Zn doped	28nm	Spherical
5 mol% Zn doped	20nm	Spherical
1 mol% Ag doped	27nm	Spherical
3 mol% Ag doped	23nm	Spherical
5 mol% Ag doped	20nm	Spherical
1 mol% Zn/Ag co- doped	23nm	Spherical
3 mol% Zn/Ag co- doped	22nm	Spherical
5 mol% Zn/Ag co- doped	21nm	Spherical

The SEM micrographs of pure TiO$_2$, 1, 3 and 5 mol% of Zn doped TiO$_2$ are shown in Fig. 5.4. The average particle size is 36nm for pure TiO$_2$ and decreases up to 20nm for doped samples. By adding Zn ions in host matrix of TiO$_2$ the size of grain shrinks. The particles are uniformly dispersed and spherical in morphology. Pure TiO$_2$ has little agglomeration and in case of doped samples the particles are uniformly arranged.
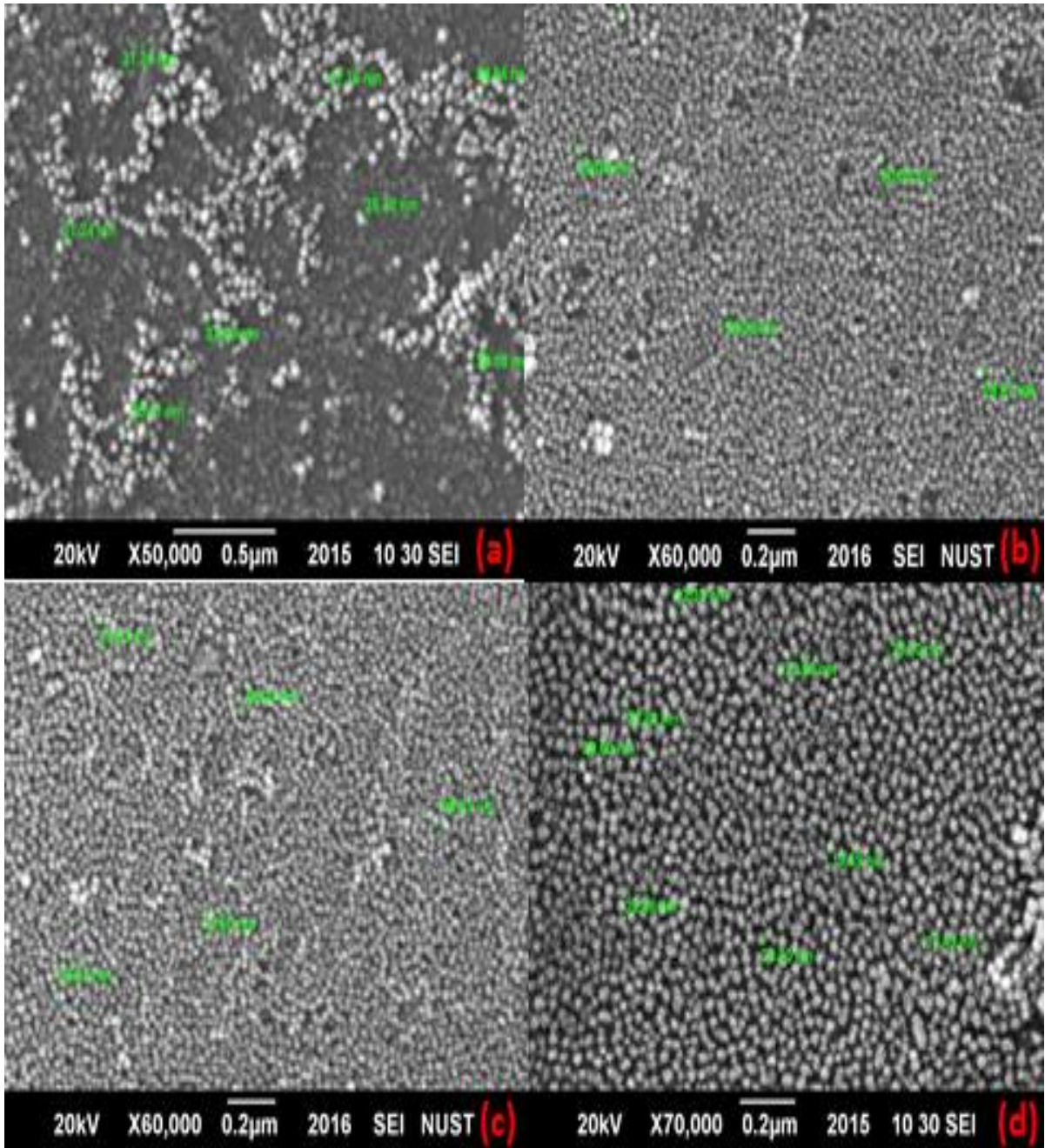
Figure 5.4- The SEM analysis of (a) TiO_2 and (b)1 mol% (c)3 mol%(d)5 mol% Zn doped TiO_2 nanoparticles

SEM analysis of Ag ions doped TiO_2 is shown in fig. 5.5. The size of doped particles decreased up to 20nm. It has been observed particle size decrease by increasing doping concentration this is because grain size decreases. Particles are spherical in shape and uniformly distributed. Initially particles have just a bit of agglomeration which is almost reduced in higher doping concentrations. The reduction in agglomeration is due to large repulsion between Ag^{1+} cations.
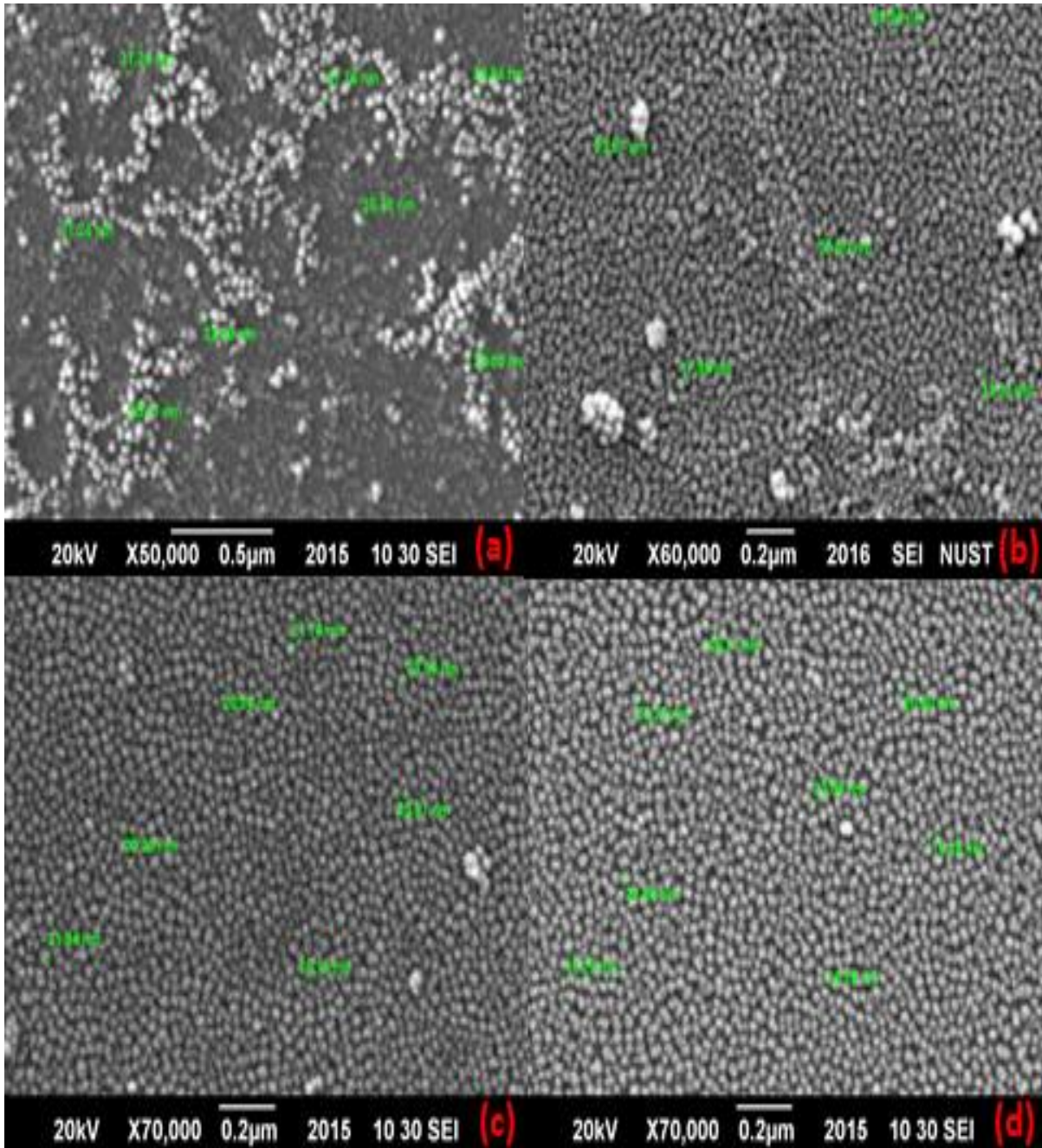
Figure 5.5- The SEM analysis of (a) TiO$_2$ and (b)1 mol% (c)3 mol%(d)5 mol% Ag doped TiO$_2$ nanoparticles

The SEM images of Zn/Ag co-doped TiO$_2$ has been showed in Fig. 5.6. The morphology is influenced by both Zn and Ag also average particle size is reduced up to 21nm by doping. A dense structure with fairly good homogeneity has obtained.
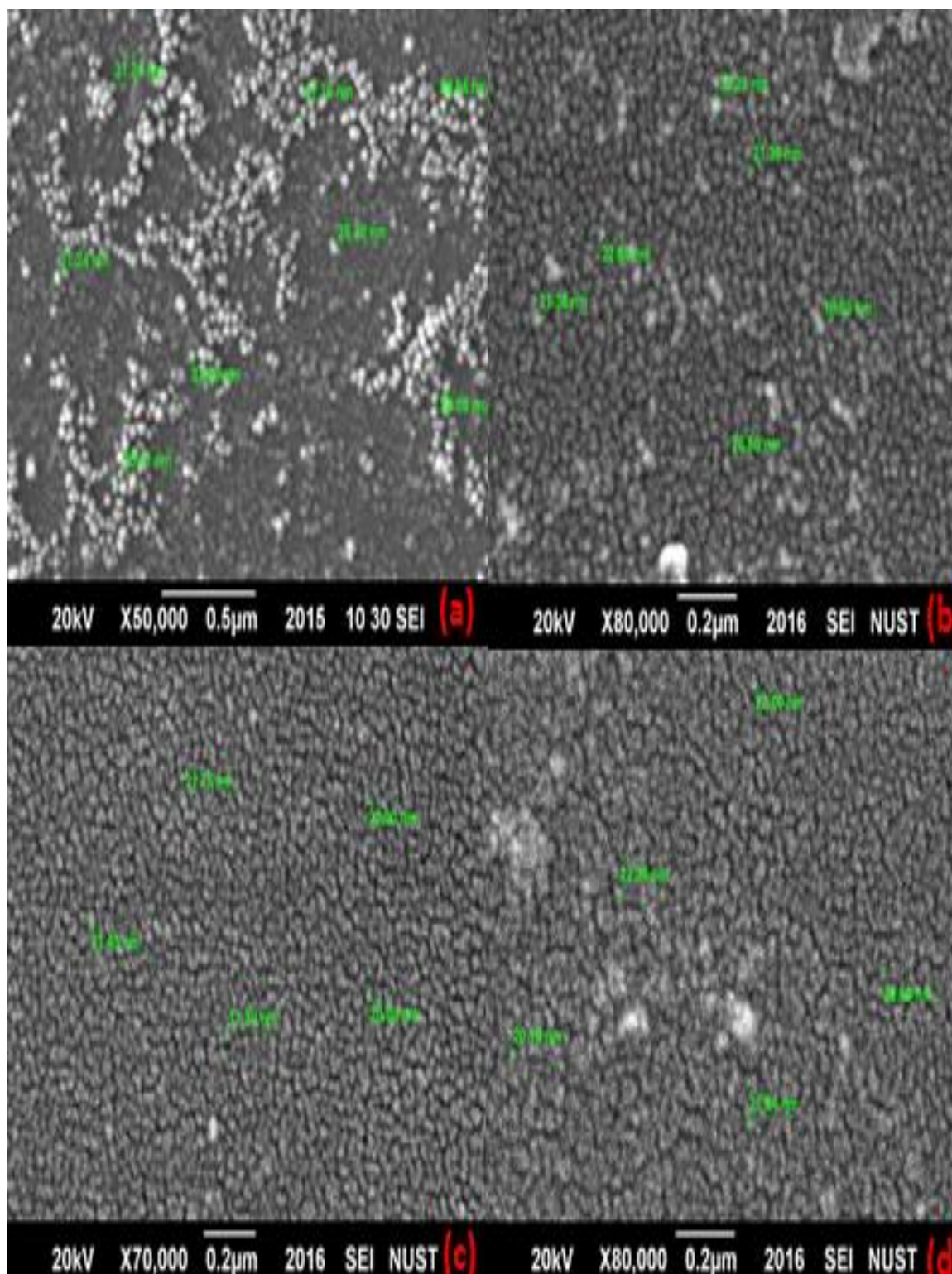
Figure 5.6- The SEM analysis of (a) TiO_2 and (b) 1 mol% (c) 3 mol% (d) 5 mol% Zn/Ag co-doped TiO_2 nanoparticles

5.3 FTIR Analysis

The different modes of vibration in synthesized TiO_2 and doped TiO_2 nanoparticles have been investigated by taking FT-IR spectra within range $400cm^{-1}$ to $4000cm^{-1}$.

The FTIR spectra of 1, 3 and 5 mol% Zn, Ag and Zn/Ag doped TiO_2 have been shown in the Fig. 5.7, 5.8 and 5.9 respectively. All samples have shown a very prominent band below 700 cm^{-1} which is associated with Ti-O stretching and bending vibrational modes. Below $1200cm^{-1}$ the broad intense band is observed which is attributed to Ti-O-Ti vibrations. By the addition of dopants the band around $600cm^{-1}$ has shown a shift towards the lower wavenumbers or higher wavelengths. It's due to the fact that dopants with higher ionic radii as compared to Ti ions shift the vibrational band towards lower wavenumber. The difference in atomic masses causes the changes in vibrations and geometry of molecules. Zn and Ag both have large atomic masses as compared to Ti and hence high electronegativity. From 1620-1635 and 2700-3600 cm^{-1} bending and stretching vibrations of O-H are observed respectively. In all samples the above mentioned bands are present and no additional band is observed which is the proof of absence of formation of secondary phases and thus suggests the successful doping of Zn, Ag, and both Zn/Ag into the host matrix of TiO_2. The results match well with previously reported results [193, 194].
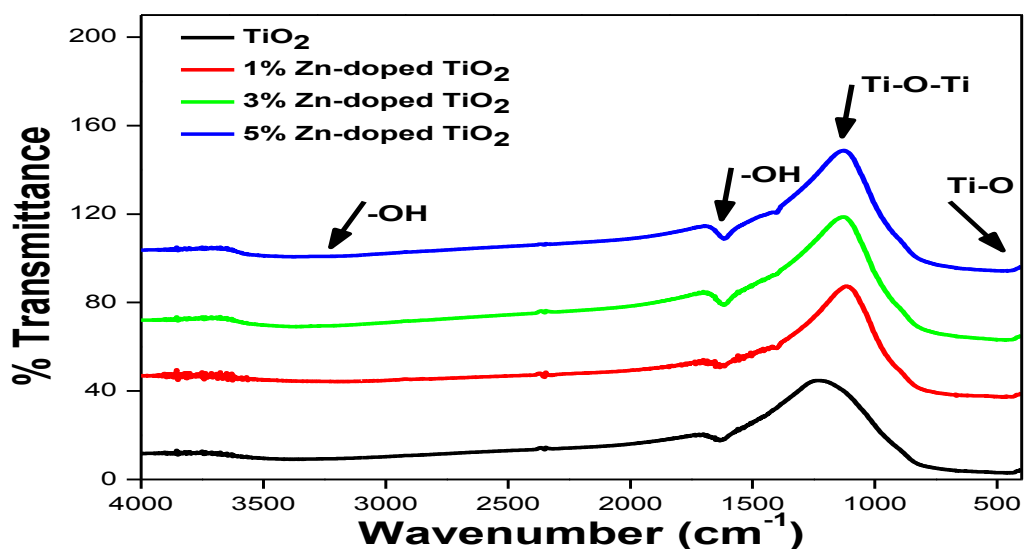
Figure 5.7- The FTIR analysis of (a) TiO_2 (b)1 mol% (c)3 mol% (d)5 mol% Zn doped TiO_2
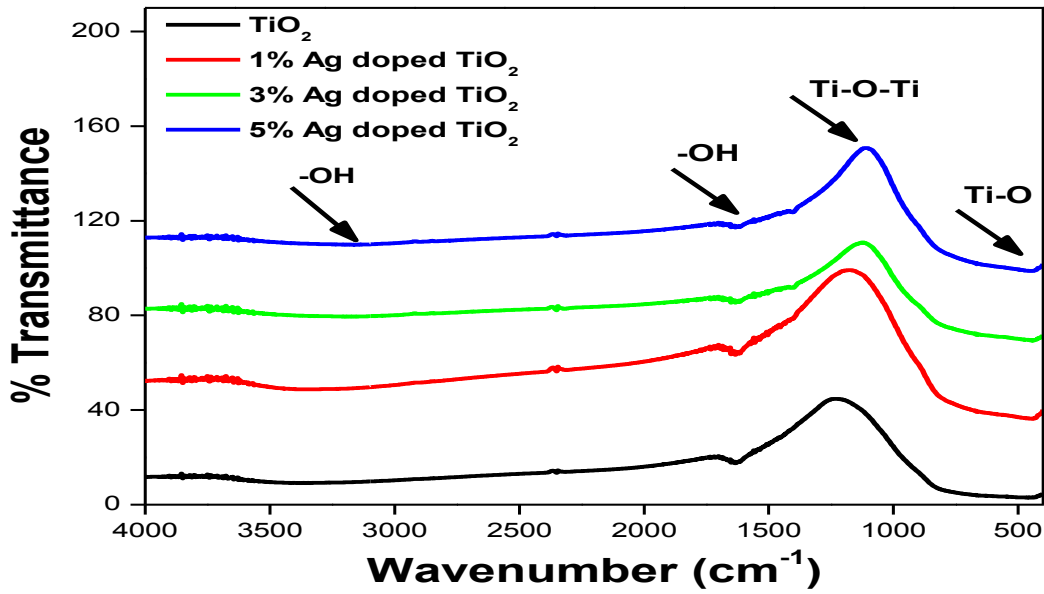
Figure 5.8- The FTIR analysis of (a) TiO$_2$ (b)1 mol% (c)3 mol% (d)5 mol% Ag doped TiO$_2$ nanoparticles
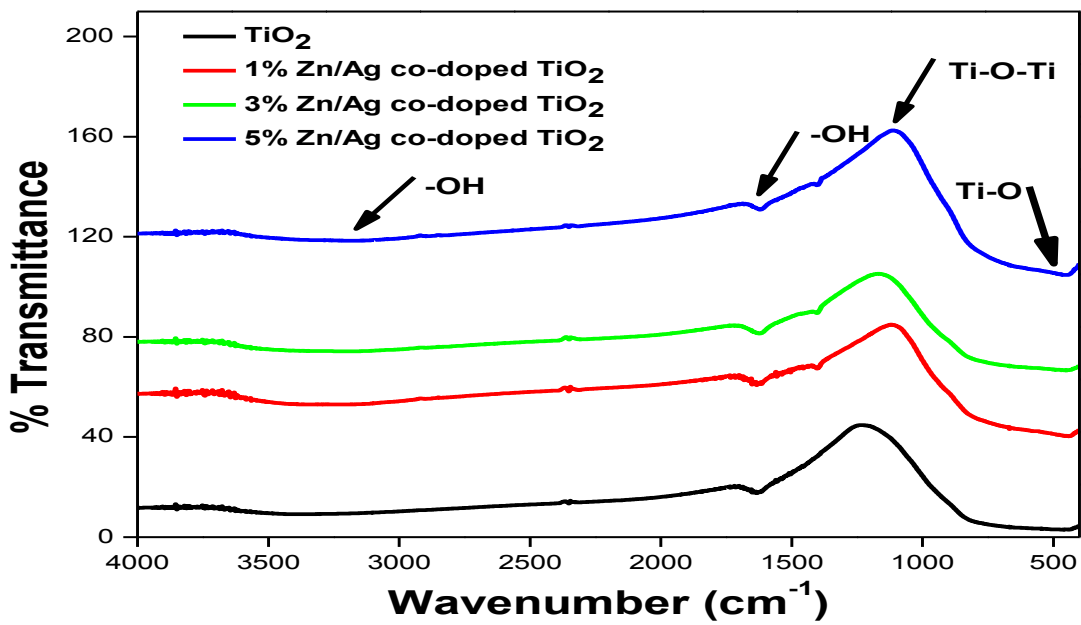
Figure 5.9- The FTIR analysis of (a) TiO$_2$ (b) 1 mol% (c) 3 mol% (d) 5 mol% Zn/Ag co-doped TiO$_2$ nanoparticles

5.4 Ultra violet/ visible (UV/Vis) spectroscopy

The optical absorption spectra has been recorded by using UV/Vis spectrophotometer in the range of 200-900nm. The absorption spectra and bandgaps of TiO_2 and 1, 3, 5 mol% Zn doped has been shown in fig. 5.10. Bandgaps has been calculated by using Manifacier model:

$$\alpha h v = A(h v - Eg)^{0.5}$$

It is cleared from spectrum due to incorporation of Zn ions the absorption band shifts towards high wavelength and bandgap decreases. This incorporation of Zn ions into TiO_2 matrix will increase its photocatalytic activity. The results match with reported results [168].
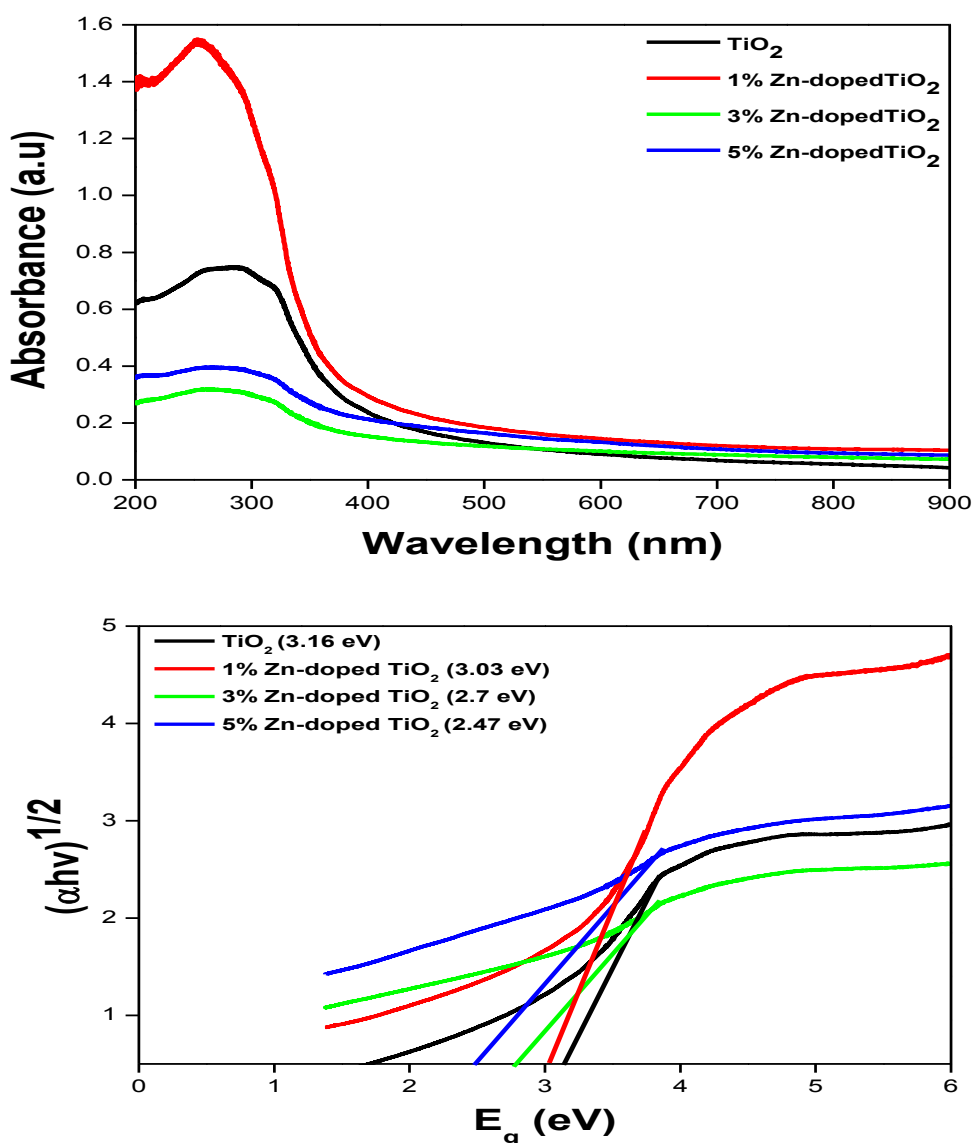
Figure 5.10- The UV/Vis spectrum and Tauc plots of (a) TiO_2 (b)1 mol% (c)3 mol% (d)5 mol% Zn doped TiO_2 nanoparticles

The UV/Vis spectra and bandgaps of 1, 3 and 5 mol% Ag doped TiO_2 has shown in fig. 5.11. It is cleared from the spectrum that by increasing doping concentration absorption band shifts towards the longer wavelength with high value of absorbance. This will increase the photocatalytic activity of TiO_2 linearly by decreasing the band gap and recombination rate. The obtained results match well with the previously reported results [195].
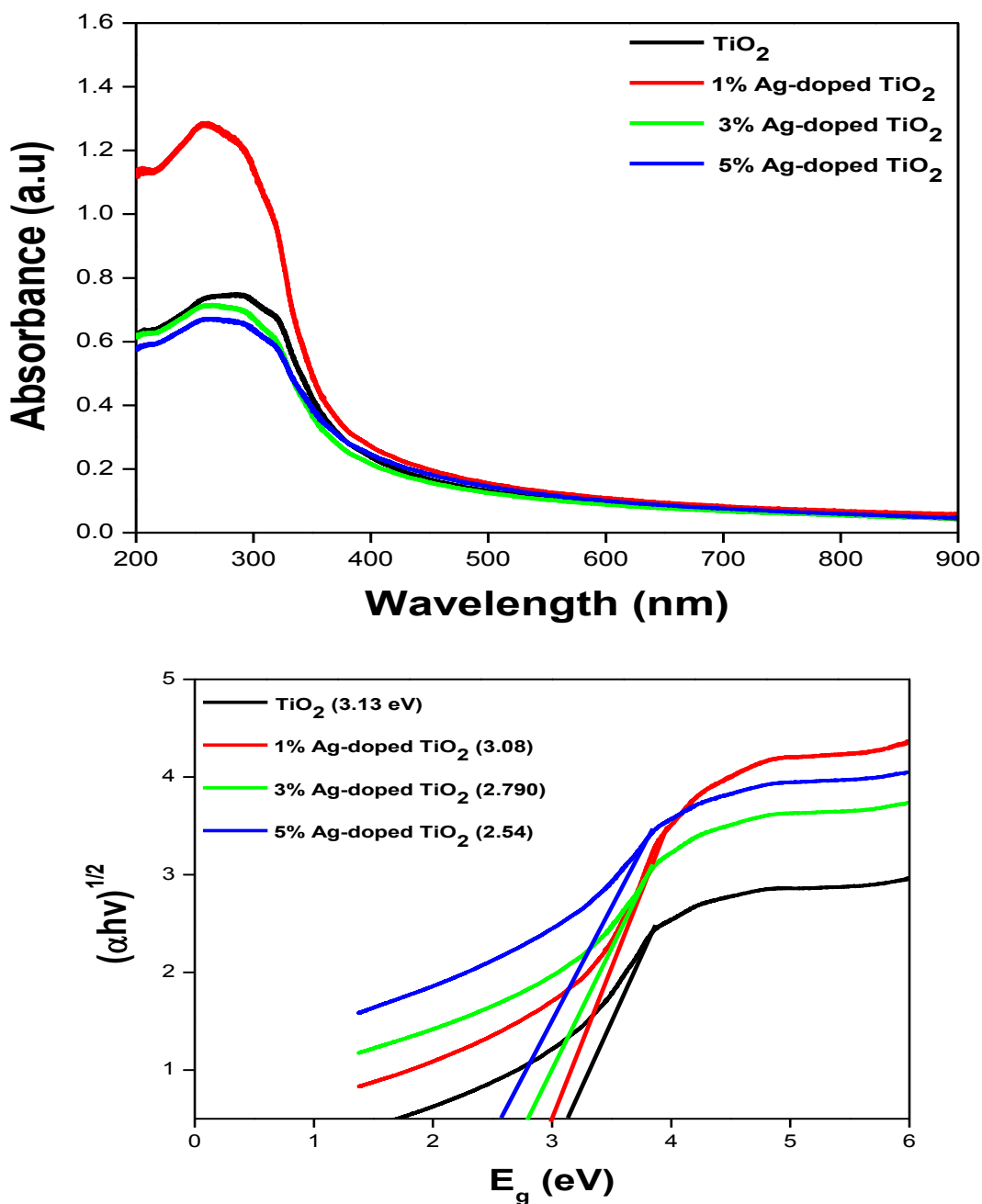
Figure 5.11- The UV/Vis spectrum and Tauc plots of (a) TiO_2 (b) 1 mol% (c) 3 mol% (d) 5 mol% Ag doped TiO_2 nanoparticles

The absorption spectra of 1, 3 and 5 mol% Zn/Ag co-doped TiO_2 is shown in fig. 5.12. From spectra it can be analyze that by increasing doping concentration the band shift towards high wavelength values linearly and bandgap decreases. Zn/Ag co-doped have high photocatalytic activity due to presence of both Zn and Ag ions as they capture more electros and prohibit the electron-hole recombination [182].
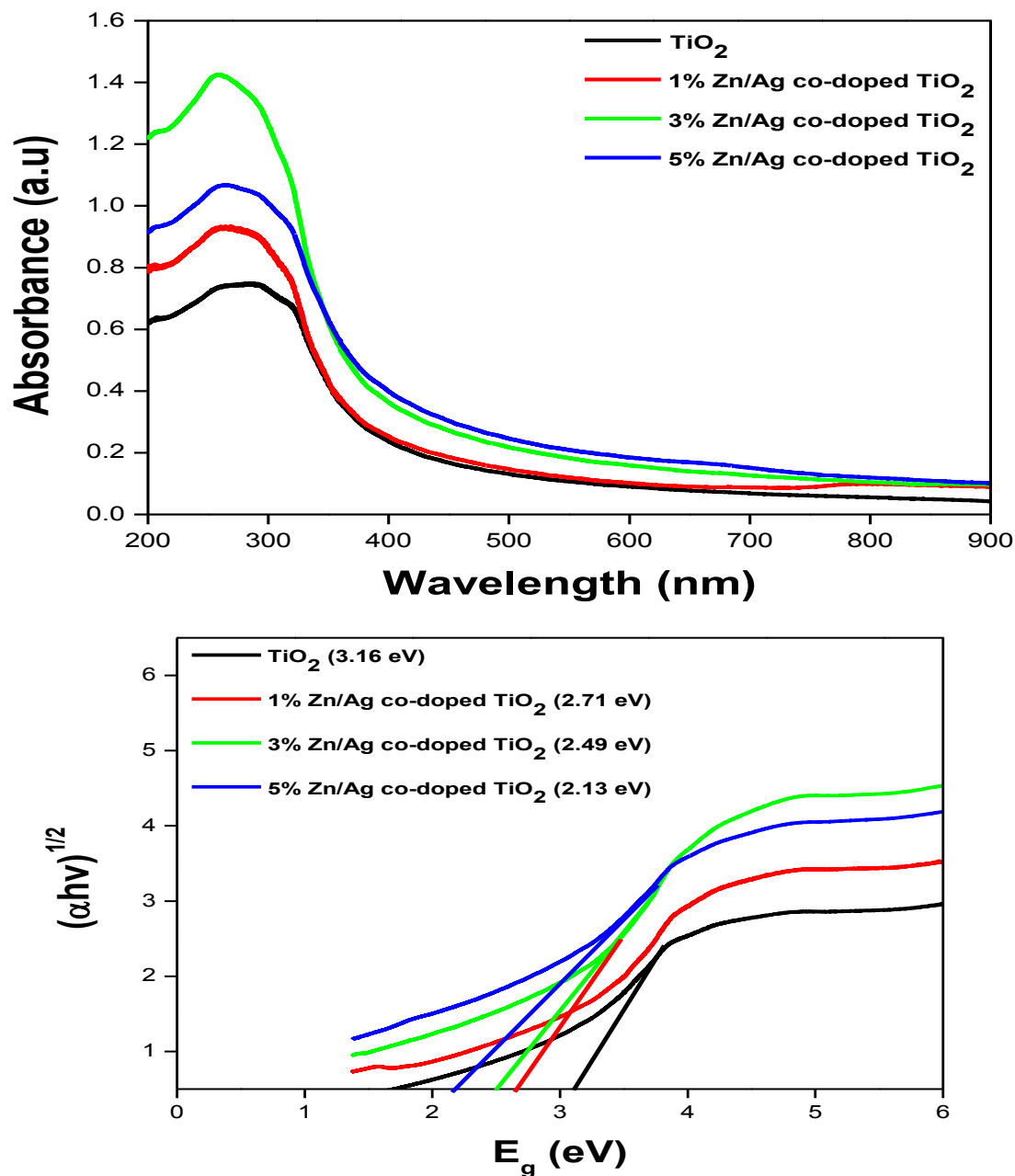
Figure 5.12- The UV/Vis spectrum and Tauc plots of (a) TiO_2 (b) 1 mol% (c) 3 mol% (d) 5 mol% Zn/Ag co-doped TiO_2 nanoparticles

5.5 Photocatalytic Evaluation

The photocatalytic activity of two commonly used textile dyes eosin y and methyl orange was carried by using four catalysts in order to choose highly efficient photocatalyst. The physical and chemical conditions for each catalyst were kept constant. It has been noticed from the spectra that 3 mol% Zn/Ag co-doped photocatalyst have highest degradation as compared to bare and single doped samples. The reason behind is both dopant have large atomic weight as compared to Ti so they decrease the bandgap energy for TiO_2 electrons also Ag ions have good properties for reducing the electron-hole recombination rate.

Zn ions doping increase the oxygen vacancies at the surface and theses vacancies induce the sub-bands below conduction band of TiO_2 and capture photo-induced electrons [168]. Theses oxygen vacancies act as scavengers. On other side Ag ions transfers the photo-induced electrons towards the oxygen vacancies immediately and increase hydroxyl radicles [196].

Variation in particle size also alters the degradation rates. Small particles have large surface to volume ratio and low electron hole recombination hence high photocatalytic activity. As 3mol% Zn/Ag co-doped photocatalyst have small particle size as compared to others. Although 3mol% Zn/Ag co-doped has small surface area but due to presence of both Zn and Ag ions it has high photocatalytic activity. The results match best with reported results [182].
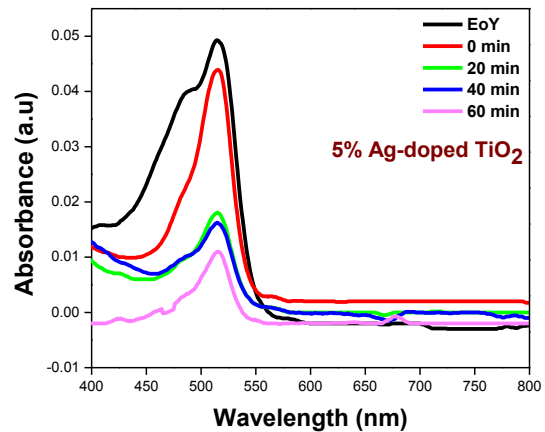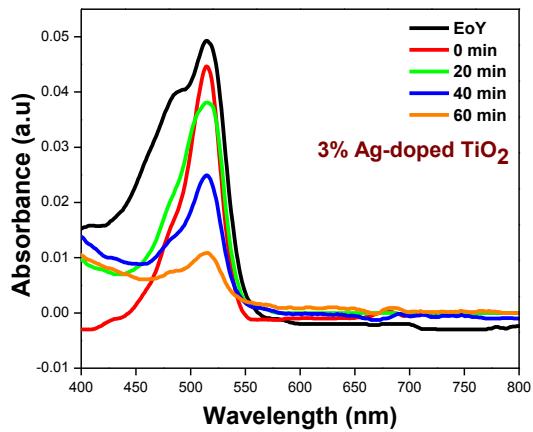
5.5.1 Degradation spectra and %degradation for Eosin Y

Different catalyst concentrations were used to degrade 5mg/L eosin y at pH 3. It was conclude that 300mg/L is the optimum concentration for degradation of eosin y. The λ_{max} for eosin y is 515nm and spectrum was recorded from 400-800nm. The recorded spectra for all four catalysts are shown below in fig. 5.13.
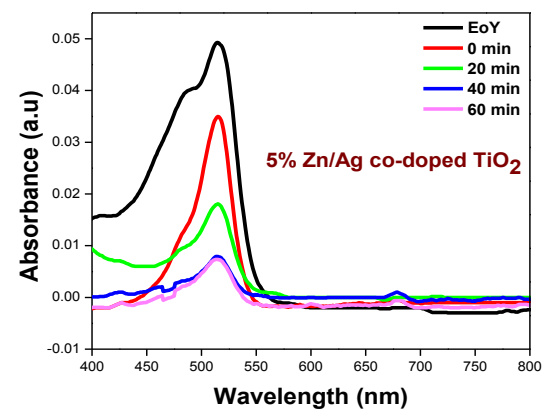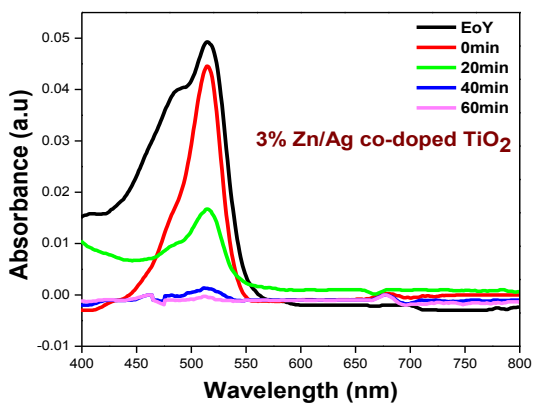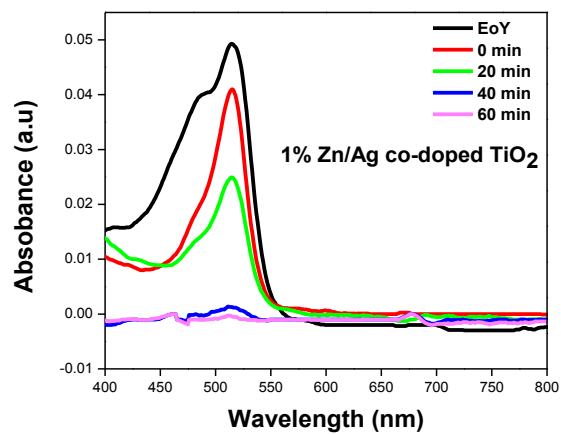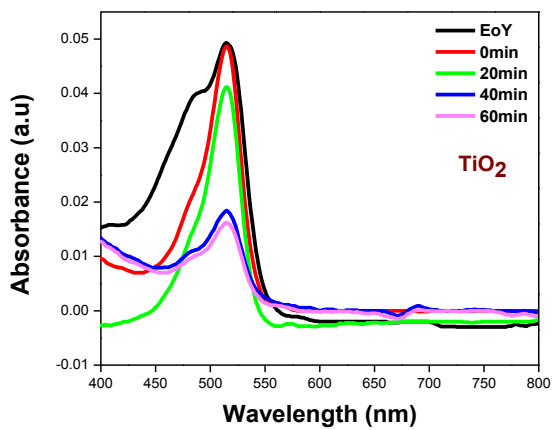
(a)

65
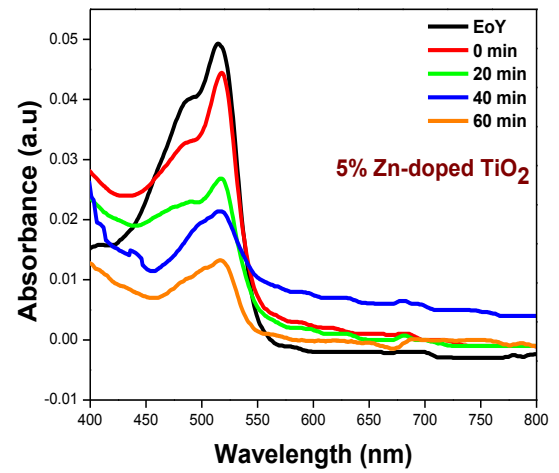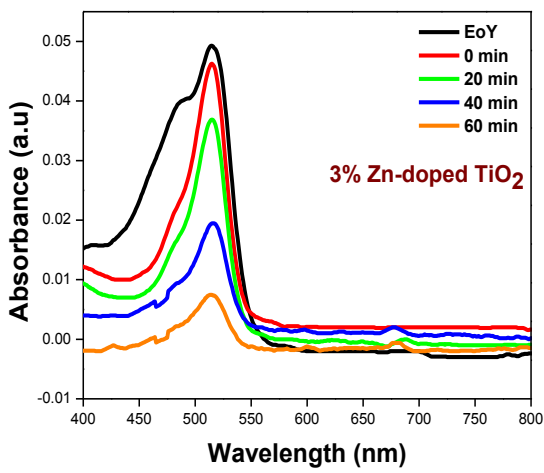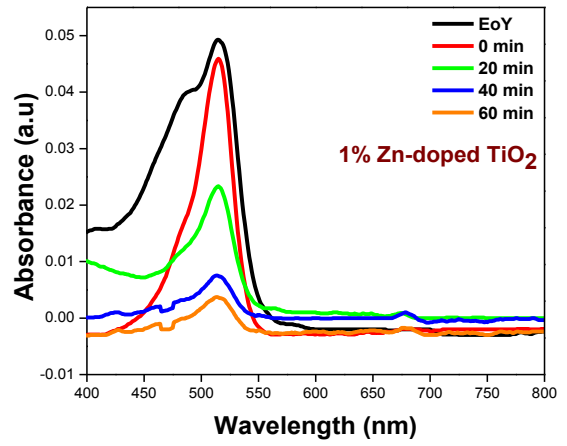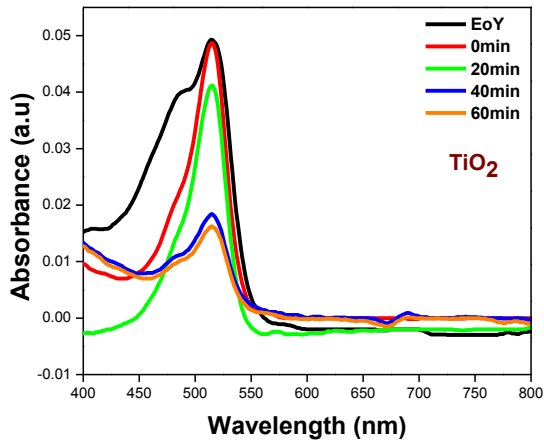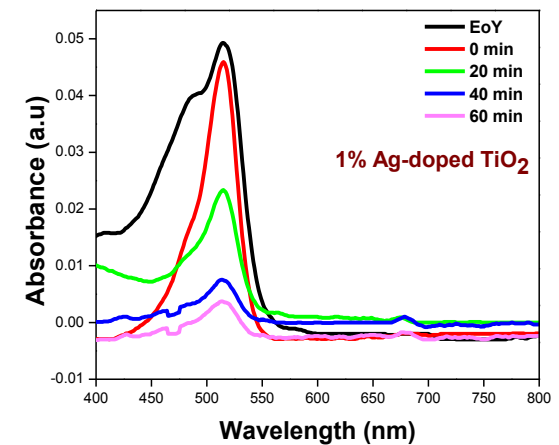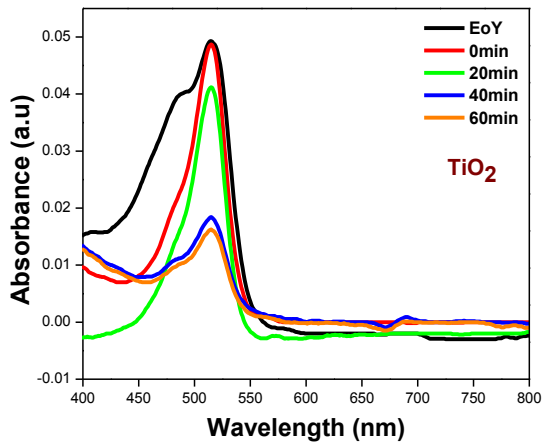
Figure 5.13- Degradation spectra of eosin y at regular intervals of time (a) Zn-doped TiO$_2$ (b) Ag-doped TiO$_2$ (c) Zn/Ag co-doped TiO$_2$
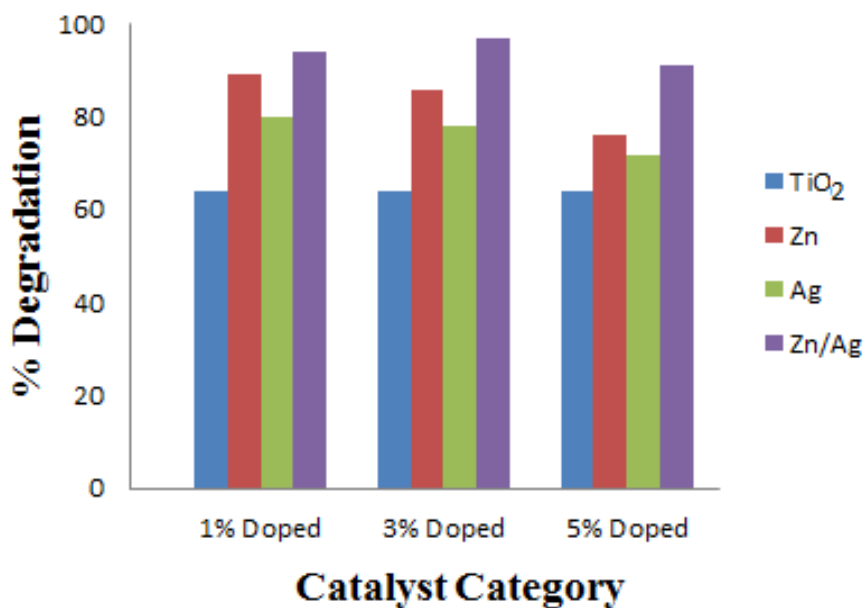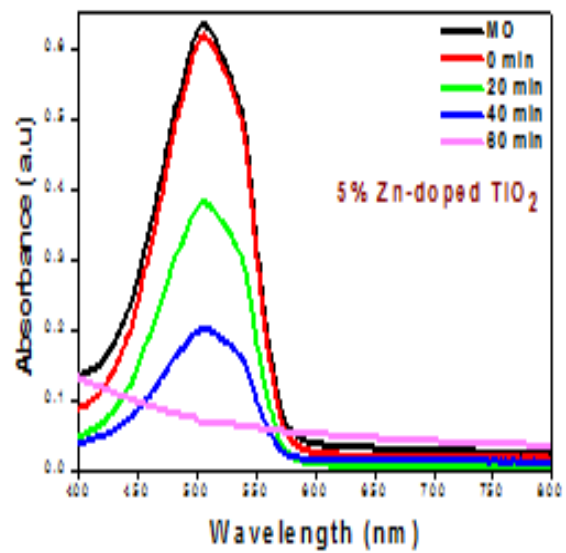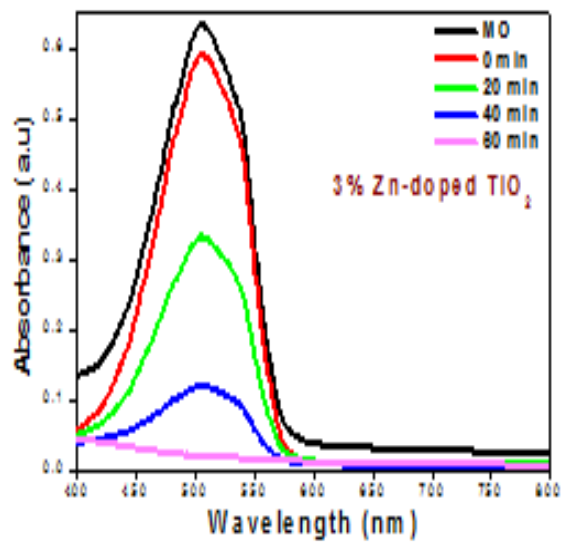
Figure 5.14- % degradation of eosin y by different catalysts

5.5.2 Degradation spectra and %degradation for Methyl orange

The optimum amount for methyl orange was selected as 500mg/L at pH3. Methyl orange is an acid base indicator and have different color at different pH and hence different λ_{max}. At pH3 methyl orange has reddish color with λmax at 504nm. The photodegradation spectrum has been shown in fig. 5.15.

(a)

68
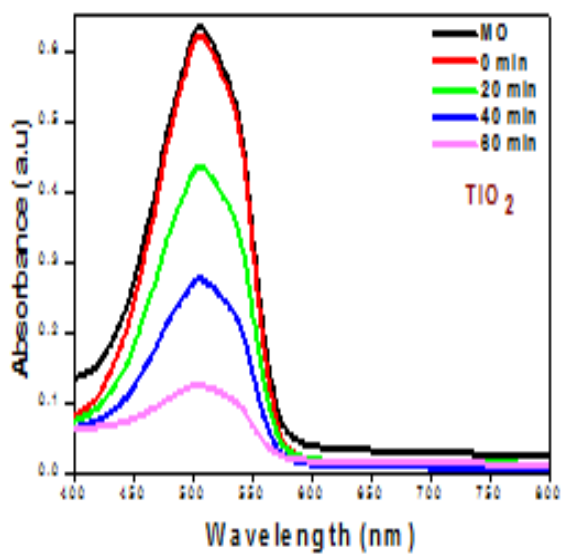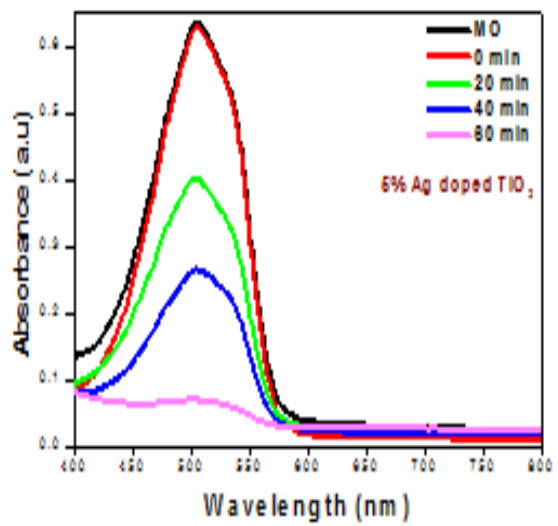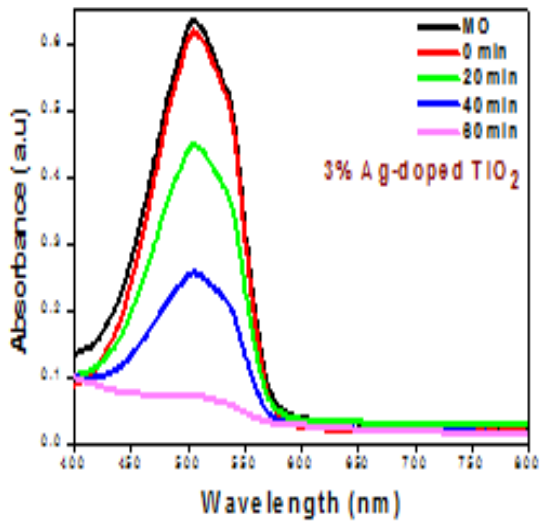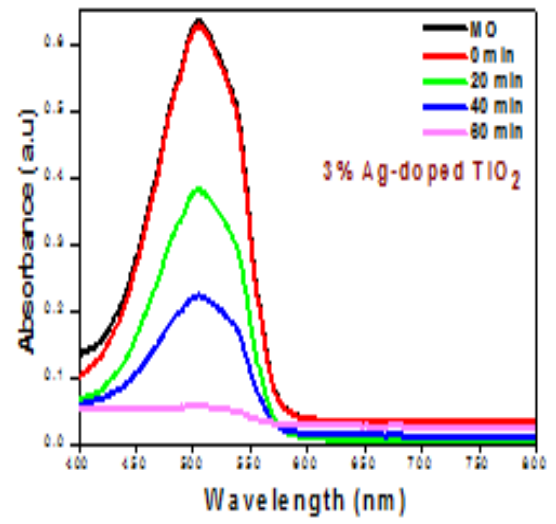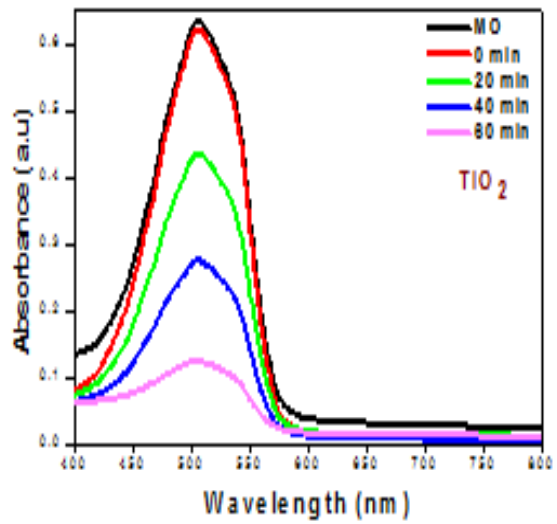
(b)
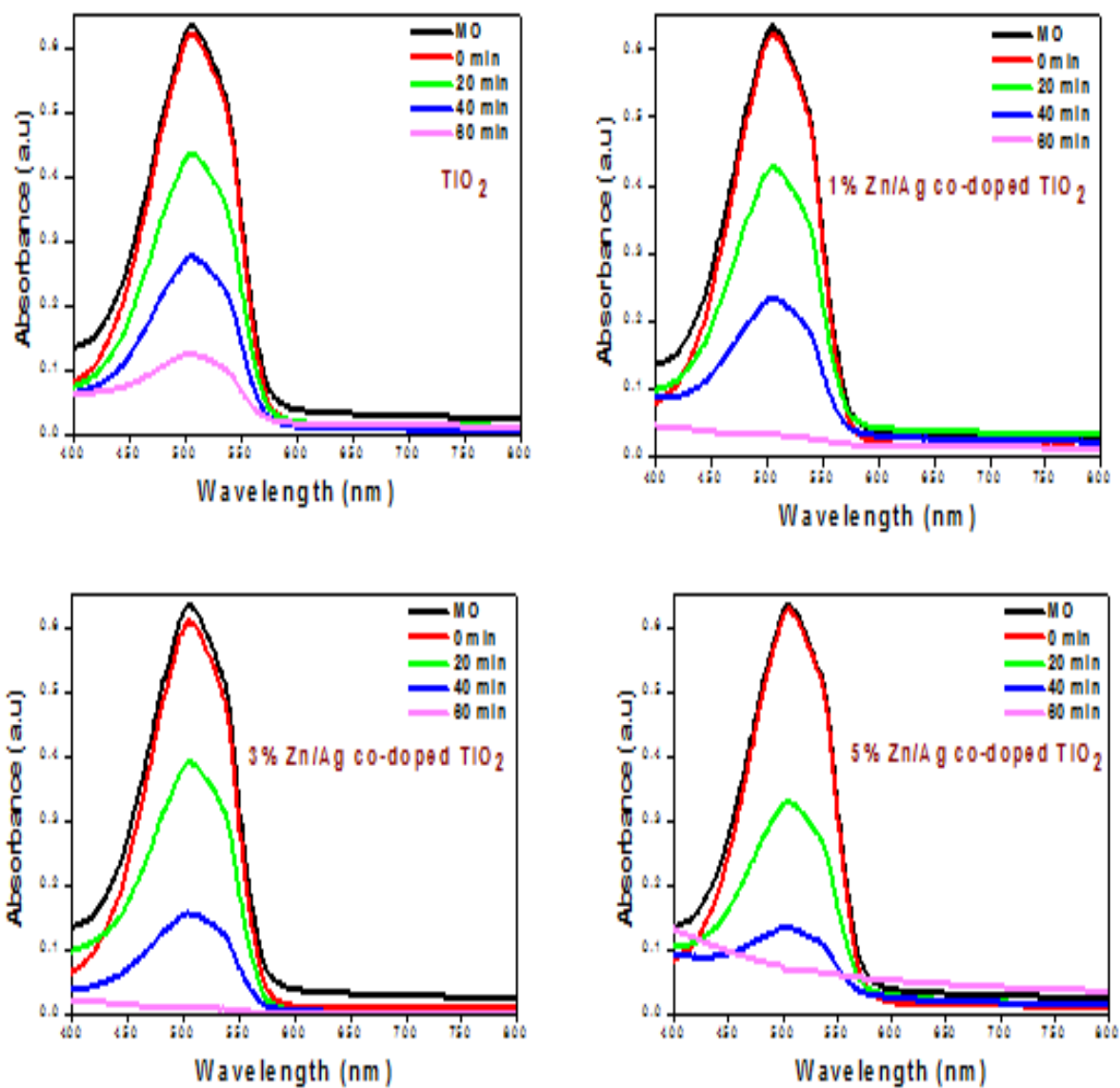
(c)

Figure 5.15- Degradation spectra of methyl orange at regular intervals of time (a) Zn-doped TiO$_2$ (b) Ag-doped TiO$_2$ (c) Zn/Ag co-doped TiO$_2$
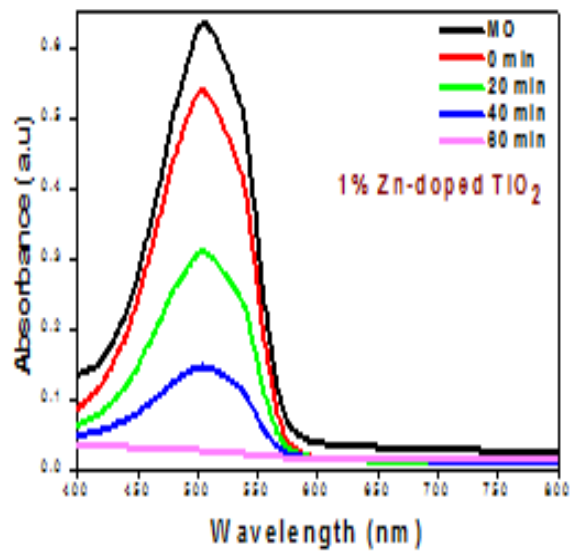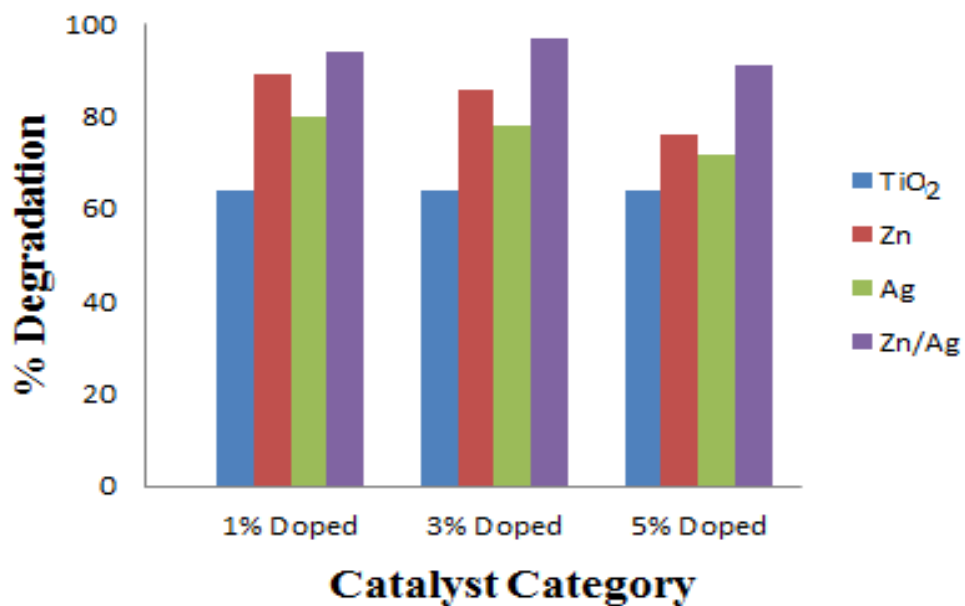
Figure 5.16- % degradation of methyl orange by different catalysts

5.5.3 Concentration decay versus time

The kinetics of methyl orange degradation is studied as a function time. The results obtained are described on the basis of Pseudo first order kinetic model because concentration of catalyst doesn't decrease during but dye concentration decreases in both cases. Concentration decay versus time is given in fig 5.17 and 5.18.
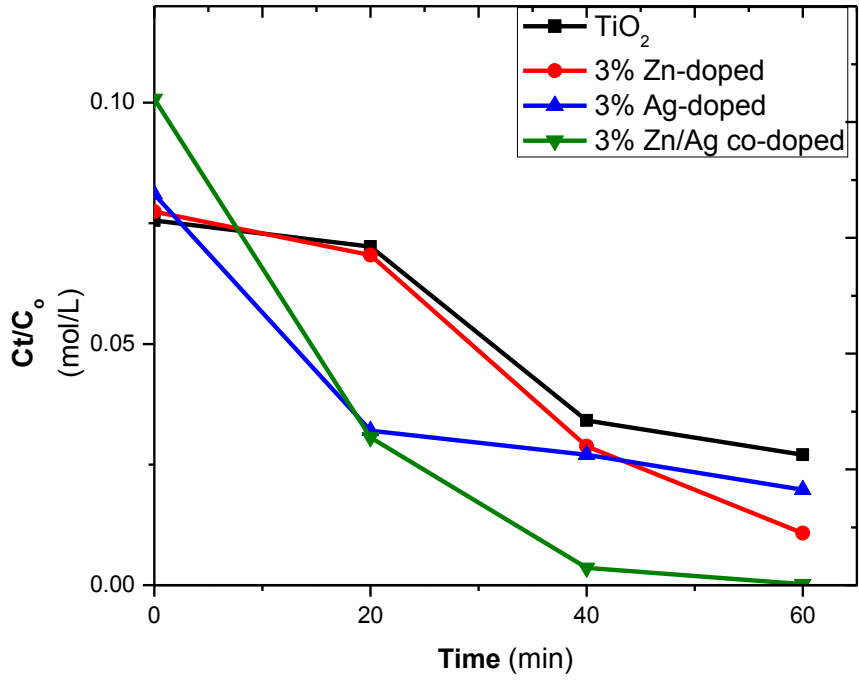
Figure 5.17- concentration versus time for eosin y
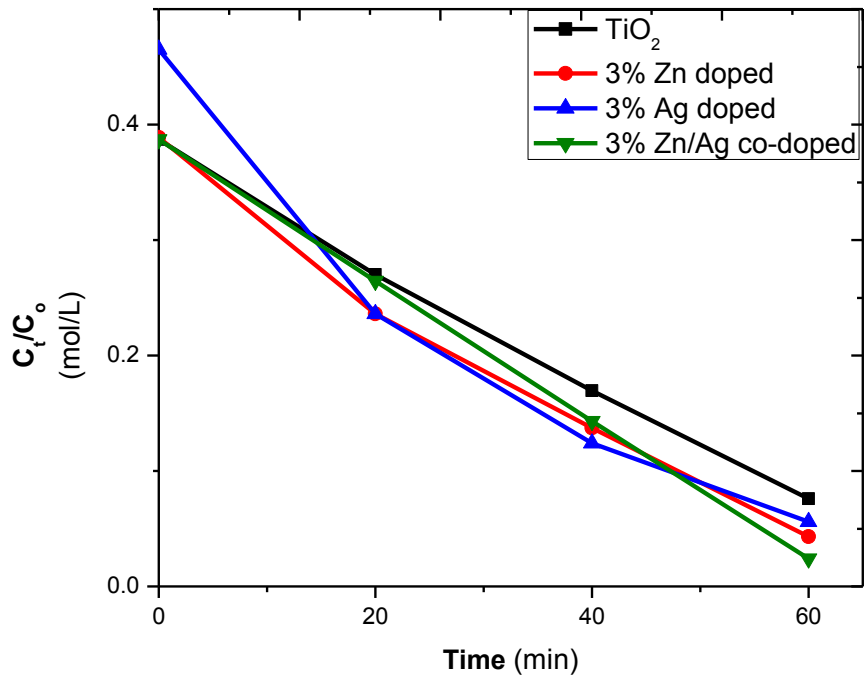
Figure 5.18- concentration versus time for methyl orange

Above figures it is clear that dye concentration with respect to time and highest degradation rate is obtained in case of 3 mol% Zn/Ag co-doped TiO$_2$. These results proof that co-doped TiO$_2$ efficiently removed dye concentration from water. It is also concluded that 3 mol% is the optimum value for doping.

Conclusion

In the present work we have successfully synthesized undoped TiO_2 nanoparticles, and Zn doped TiO_2 nanoparticles, Ag doped TiO_2 nanoparticles, and Zn/Ag co-doped TiO_2 nanoparticles with different percentages 1%, 3%, and 5% in each case. In all the cases the sol-gel route has been adopted for the synthesis of all the samples. The prepared samples have been characterized by using different characterization techniques. In order to study the crystalline structure of the samples XRD analysis has confirmed the formation of anatase phase of TiO_2 nanoparticles and Zn doped TiO_2 nanoparticles. However the XRD analysis have shown that increasing the Ag content in the TiO_2 host matrix has induced brookite phase of titania to a small extent. The morphology of all the prepared samples has been investigated by using scanning electron microscopy. Pure TiO_2 and all the Zn, Ag, and Zn/Ag co-doped TiO_2 have shown spherical morphology with particle size ranging from 20-29 nm. The vibrational modes have been investigated by FT-IR spectroscopy have shown the presence of bands around 600 cm^{-1} thus confirming the Ti-O-Ti bond formation. The photocatalytic activity of all the samples has been investigated for organic dyes like eosin y and methyl orange. It has been found that the both dyes have been completely degraded within 60 minutes under the irradiation of UV-light. The 3% Zn, Ag and Zn/Ag co-doped samples have shown degradation upto 86%, 75%, and 98% in 60 minutes for eosin y which is much better than 61% degradation as obtained by undoped TiO_2.

In similar manner the 3% Zn, Ag and Zn/Ag co-doped samples have shown degradation upto 93%, 91%, and 95% in 60 minutes for methyl orange which is much better than 80% degradation as obtained by undoped TiO_2.

Thus it can be concluded that photocatalytic activity of TiO_2 can significantly improve by using Zn, Ag, and Zn/Ag co-doped TiO_2 nanoparticles.

References

1. S. J. L. Billinge, Journal of Solid State Chemistry **181** (7), 1695-1700 (2008).

2. K. E. Drexler, Bulletin of Science, Technology and Society **24** (1), 21-27 (2004).

3. E. Serrano, G. Rus and J. García-Martínez, Renewable and Sustainable Energy Reviews **13** (9), 2373-2384 (2009).

4. S. Eustis and M. A. el-Sayed, Chemical Society reviews **35** (3), 209-217 (2006).

5. N. Taniguchi, (1974).

6. E. Roduner, Chemical Society reviews **35** (7), 583-592 (2006).

7. S. M. Naidu and N. S. Mani, *Applied Physics*. (Pearson Education, 2009).

8. A. M. Glezer, Russian Metallurgy (Metally) **2011** (4), 263-269 (2011).

9. D. D. A. Zweck, (Future technologies divison of VDI, technologiezentrum GmbH graf reeke, (2004) 119.

10. G. M. a. T. Ganguly, Indian J. Phys. **85**, 1229-1245 (2011).

11. N. Scott and H. Chen, Industrial Biotechnology **9** (1), 17-18 (2013).

12. M. M. Khin, A. S. Nair, V. J. Babu, R. Murugan and S. Ramakrishna, Energy & Environmental Science **5** (8), 8075 (2012).

13. M. T. Harrison, S. V. Kershaw, M. G. Burt, A. L. Rogach, A. Kornowski, A. Eychmüller and H. Weller, Pure and Applied Chemistry **72** (1-2) (2000).

14. P. L. McEuen, Nature **393** (6680), 15-17 (1998).

15. Y. Malam, M. Loizidou and A. M. Seifalian, Trends in pharmacological sciences **30** (11), 592-599 (2009).

16. K. Nakata and A. Fujishima, Journal of Photochemistry and Photobiology C: Photochemistry Reviews **13** (3), 169-189 (2012).

17. M. Wang and M. Thanou, Pharmacological research **62** (2), 90-99 (2010).

18. J. Tian, K. K. Wong, C. M. Ho, C. N. Lok, W. Y. Yu, C. M. Che, J. F. Chiu and P. K. Tam, Chem. Med. Chem **2** (1), 129-136 (2007).

19. R. Dastjerdi, M. Montazer and S. Shahsavan, Colloids and surfaces. B, Biointerfaces **81** (1), 32-41 (2010).

20. J. Domaradzki, M. M. , K. S. , D. Wojcieszak and B. A. , Optica Application **XLIII** (2013).

21. W. Wenliang and H. Honggang, Chinese Optics Letters **8** (S1), 35-37 (2010).

22. X. Chen and S. S. Mao, Chemical reviews **107** (7), 2891-2959 (2007).

23. W. L. XUXU WANG, XIANZHI FU, BASSET J.-M., LEFEBVRE F., Journal of Catalysis **238(1)**, 13 (2006).

24. J. Yu, G. Wang, B. Cheng and M. Zhou, Applied Catalysis B: Environmental **69** (34), 171-180 (2007).

25. O. Carp, Progress in Solid State Chemistry **32** (1-2), 33-177 (2004).

26. H. K. Cromer D T, J Am Chem Soc **77**, 2 (1955).

27. B. V. W. H., Acta Crystallogr **16**, 3 (1961).

28. S.-D. Mo and W. Y. Ching, Physical Review B **51** (19), 13023-13032 (1995).

29. O. T. Wunderlich W, Miao L, et al, J Ceram Process Res **5**, 12 (2004).

30. S. M. Gupta and M. Tripathi, Chinese Science Bulletin **56** (16), 1639-1657 (2011).

31. U. Diebold, Surface Science Reports **48** (5-8), 53-229 (2003).

32. D. A. H. Hanaor and C. C. Sorrell, Journal of Materials Science **46** (4), 855-874 (2010).

33. D. F. Simons P Y, Acta Cryst **23**, 3 (1967).

34. P. C, high temperatures-high pressure **8**, 6 (1976).

35. R. Ren, Journal of Materials Science **35** (23), 6015-6026 (2000).

36. T. Arlt, M. Bermejo, M. A. Blanco, L. Gerward, J. Z. Jiang, J. Staun Olsen and J. M. Recio, Physical Review B **61** (21), 14414-14419 (2000).

37. J. Muscat, V. Swamy and N. M. Harrison, Physical Review B **65** (22) (2002).

38. E. T. Fisher J, in *Othmer encyclopaedia of chemical technology.* (Wiley, New York, (2001).

39. A. Maldotti and A. Molinari, Topics in current chemistry **303**, 185-216 (2011).

40. L. Sun, L. Huo, H. Zhao, S. Gao and J. Zhao, Sensors and Actuators B: Chemical **114** (1), 387-391 (2006).

41. J. Nowotny, C. C. Sorrell, L. R. Sheppard and T. Bak, International Journal of Hydrogen Energy **30** (5), 521-544 (2005).

42. M. Gratzel, Nature **414** (6861), 338-344 (2001).

43. S. K. Poznyak, M. L. Zheludkevich, D. Raps, F. Gammel, K. A. Yasakau and M. G.S. Ferreira, Progress in Organic Coatings **62** (2), 226-235 (2008).

44. M. R. A. Gregory M Harry, Andres E Becerra-Toledo, Helena Armandula, Eric Black, Kate Dooley, Matt Eichenfield, Chinyere Nwabugwu, Akira Villar, D R M Crooks, Classical and Quantum Gravity **24** (2006).

45. B. M. Q Fan, A K Ray, M L Turner and A B Seddon, Journal of Physics D: Applied Physics **33**.

46.   D. Zhao, T. Peng, J. Xiao, C. Yan and X. Ke, Materials Letters **61** (1), 105-110 (2007).

47.   R. G. Salomon, Tetrahedron **39** (4), 485-575 (1983).

48.   H. Sakai, R. Baba, K. Hashimoto, A. Fujishima and A. Heller, The Journal of Physical Chemistry **99** (31), 11896-11900 (1995).

49.   A. Fujishima and K. Honda, Nature **238** (5358), 37-38 (1972).

50.   A. Kudo and Y. Miseki, Chemical Society reviews **38** (1), 253-278 (2009).

51.   K. Maeda, Journal of Photochemistry and Photobiology C: Photochemistry Reviews **12** (4), 237-268 (2011).

52.   R. Abe, Journal of Photochemistry and Photobiology C: Photochemistry Reviews **11** (4), 179- 209 (2010).

53.   K. A. W. L. Caballero, N.S. Allen, J. Verran, J. Photochem. Photobiol. A **202**, 7 (2009).

54.   T. Matsunaga, R. Tomoda, T. Nakajima and H. Wake, FEMS Microbiology Letters **29** (1-2), 211-214 (1985).

55.   K. Sunada, T. Watanabe and K. Hashimoto, Journal of Photochemistry and Photobiology A: Chemistry **156** (1-3), 227-233 (2003).

56.   A. Fujishima, X. Zhang and D. Tryk, International Journal of Hydrogen Energy **32** (14), 2664-2672 (2007).

57.   K. Nakata, B. Liu, Y. Ishikawa, M. Sakai, H. Saito, T. Ochiai, H. Sakai, T. Murakami, M. Abe, K. Takagi and A. Fujishima, Chemistry Letters **40** (10), 1107-1109 (2011).

58.   A. Janczyk, E. Krakowska, G. Stochel and W. Macyk, J Am Chem Soc **128** (49), 15574-15575 (2006).

59.   Y. Nosaka, T. Daimon, A. Y. Nosaka and Y. Murakami, Physical Chemistry Chemical Physics **6** (11), 2917 (2004).

60.   A. Fujishima and X. Zhang, Comptes Rendus Chimie **9** (5-6), 750-760 (2006).

61.   R. Wang, K. Hashimoto, A. Fujishima, M. Chikuni, E. Kojima, A. Kitamura, M. Shimohigoshi and T. Watanabe, Advanced Materials **10** (2), 135-138 (1998).

62.   H. Haick and Y. Paz, The Journal of Physical Chemistry B **105** (15), 3045-3051 (2001).

63.   W. Kubo and T. Tatsuma, Journal of Materials Chemistry **15** (30), 3104 (2005).

64.   A. Mills, N. Elliott, G. Hill, D. Fallis, J. R. Durrant and R. L. Willis, Photochemical & Photobiological Sciences **2** (5), 591 (2003).

65.   H. S. Mills A, Lee SK, Res Chem Intermed **31** (2004).

66. O. Y. Ohtani B, Nishimoto S., J Phys Chem B **101**, 7 (1993).

67. A. Sclafani and J. M. Herrmann, The Journal of Physical Chemistry **100** (32), 13655-13661 (1996).

68. M. Anpo and P. V. Kamat, (2010).

69. M. J. Gázquez, J. P. Bolívar, R. Garcia-Tenorio and F. Vaca, Materials Sciences and Applications **05** (07), 441-458 (2014).

70. J. a. E. Fisher, T.A., in Kirk-Othmer Encyclopedia of Chemical Technology, John Wiley & Sons, New York. (2001).

71. H. T. Burdett JK, J Am Chem Soc **109** (1987).

72. H. T, (Reidel, Dordrecht, 1988).

73. G. L. Beltrán A1, Andrés J, J Phys Chem B. **110** (2006).

74. L. M. F. Arias, A. A. Duran, D. Cardona, E. Camps, M. E. Gómez and G. Zambrano, Journal of Physics: Conference Series **614**, 012008 (2015).

75. N. Daude, C. Gout and C. Jouanin, Physical Review B **15** (6), 3229-3235 (1977).

76. T. Ohno, K. Sarukawa and M. Matsumura, The Journal of Physical Chemistry B **105** (12), 2417-2420 (2001).

77. H. Wang and J. P. Lewis, Journal of Physics: Condensed Matter **18** (2), 421-434 (2006).

78. S. T. Aruna, M. Muniprakash and V. K. William Grips, Journal of Applied Electrochemistry **43** (8), 805-815 (2013).

79. D. Reyes-Coronado, G. Rodriguez-Gattorno, M. E. Espinosa-Pesqueira, C. Cab, R. de Coss and G. Oskam, Nanotechnology **19** (14), 145605 (2008).

80. T. N. R. Akira Fujishima∗, Donald A. Tryk, Journal of Photochemistry and Photobiology C: Photochemistry Reviews **1**, 22 (2000).

81. L. Zhang and Y. Zhu, Catalysis Science & Technology **2** (4), 694 (2012).

82. K. Song, J. Zhou, J. Bao and Y. Feng, Journal of the American Ceramic Society **91** (4), 1369-1371 (2008).

83. Z. Ambrus, N. Balázs, T. Alapi, G. Wittmann, P. Sipos, A. Dombi and K. Mogyorósi, Applied Catalysis B: Environmental **81** (1-2), 27-37 (2008).

84. G. K. Mor, O. K. Varghese, M. Paulose, K. Shankar and C. A. Grimes, Solar Energy Materials and Solar Cells **90** (14), 2011-2075 (2006).

85. M. Pelaez, N. T. Nolan, S. C. Pillai, M. K. Seery, P. Falaras, A. G. Kontos, P. S. M. Dunlop, J. W. J. Hamilton, J. A. Byrne, K. O'Shea, M. H. Entezari and D. D.

Dionysiou, Applied Catalysis B: Environmental **125**, 331-349 (2012).

86.   A. L. Castro, M. R. Nunes, M. D. Carvalho, L. P. Ferreira, J. C. Jumas, F. M. Costa and M. H. Florêncio, Journal of Solid State Chemistry **182** (7), 1838-1845 (2009).

87.   R. J. Tayade, R. G. Kulkarni and R. V. Jasra, Industrial & Engineering Chemistry Research **45** (15), 5231-5238 (2006).

88.   M. M. Joshi, N. K. Labhsetwar, P. A. Mangrulkar, S. N. Tijare, S. P. Kamble and S. S. Rayalu, Applied Catalysis A: General **357** (1), 26-33 (2009).

89.   R. Asahi, T. Morikawa, H. Hazama and M. Matsubara, Journal of physics. Condensed matter : an Institute of Physics journal **20** (6), 064227 (2008).

90.   K. Szacilowski, W. Macyk, A. Drzewiecka-Matuszek, M. Brindell and G. Stochel, Chemical reviews **105** (6), 2647-2694 (2005).

91.   H. P. Maruska and A. K. Ghosh, Solar Energy Materials **1** (3-4), 237-247 (1979).

92.   T. Tian, J. Hu and Z. Xiao, World Journal of Nano Science and Engineering **04** (04), 111-125 (2014).

93.   M. A. Khan, D. H. Han and O. B. Yang, Applied Surface Science **255** (6), 3687-3690 (2009).

94.   J. Gautron, P. Lemasson and J.-F. Marucco, Faraday Discussions of the Chemical Society **70**, 81 (1980).

95.   B. Xin, Z. Ren, P. Wang, J. Liu, L. Jing and H. Fu, Applied Surface Science **253** (9), 4390-4395 (2007).

96.   M. Bellardita, M. Addamo, A. Di Paola and L. Palmisano, Chemical Physics **339** (13), 94-103 (2007).

97.   C. Burda, Y. Lou, X. Chen, A. C. S. Samia, J. Stout and J. L. Gole, Nano Letters **3** (8), 1049-1051 (2003).

98.   M. A. Behnajady and H. Eskandarloo, Journal of Nanoscience and Nanotechnology **13** (1), 548-553 (2013).

99.   C. Rath, P. Mohanty, A. C. Pandey and N. C. Mishra, Journal of Physics D: Applied Physics **42** (20), 205101 (2009).

100.   R. Vogel, P. Hoyer and H. Weller, The Journal of Physical Chemistry **98** (12), 3183-3188 (1994).

101.   H. Zhang and J. F. Banfield, Journal of Materials Research **15** (02), 437-448 (2011).

102.   Y. Ahn, Materials Letters **57** (30), 4660-4666 (2003).

103.   K.-N. P. Kumar, K. Keizer, A. J. Burggraaf, T. Okubo and H. Nagamoto, Journal of Materials Chemistry **3** (11), 1151 (1993).

104.	J. Arbiol, J. Cerdà, G. Dezanneau, A. Cirera, F. Peiró, A. Cornet and J. R. Morante, Journal of Applied Physics **92** (2), 853 (2002).

105.	G. Li, L. Li, J. Boerio-Goates and B. F. Woodfield, J Am Chem Soc **127** (24), 8659-8666 (2005).

106.	L. Gerward and J. Staun Olsen, Journal of Applied Crystallography **30** (3), 259-264 (1997).

107.	A. Mineralogist, (1976), Vol. 61, pp. 6.

108.	N. Serpone, J Phys Chem B **110** (48), 24287-24293 (2006).

109.	K. I. Hadjiivanov and D. G. Klissurski, Chemical Society reviews **25** (1), 61 (1996).

110.	M. I. Franch, J. Peral, X. Domenech and J. A. Ayllon, Chemical communications (14), 1851-1853 (2005).

111.	K. T. Ranjit, H. Cohen, I. Willner, S. Bossmann and A. M. Braun, Journal of Materials Science **34** (21), 5273-5280 (1999).

112.	D. J. Reidy, J. D. Holmes and M. A. Morris, Journal of the European Ceramic Society **26** (9), 1527-1534 (2006).

113.	R. Janes, Dyes and Pigments **62** (3), 199-212 (2004).

114.	S. Riyas, G. Krishnan and P. N. M. Das, Advances in Applied Ceramics **106** (5), 255-264 (2007).

115.	R. D. Shannon and J. A. Pask, Journal of the American Ceramic Society **48** (8), 391-398 (1965).

116.	S. Vargas, R. Arroyo, E. Haro and R. Rodríguez, Journal of Materials Research **14** (10), 3932-3937 (2011).

117.	A. Zaleska, Recent Patents on Engineering **2** (3), 157-164 (2008).

118.	S. Karvinen, Solid State Sciences **5** (5), 811-819 (2003).

119.	M. A. Debeila, M. C. Raphulu, E. Mokoena, M. Avalos, V. Petranovskii, N. J. Coville and M. S. Scurrell, Materials Science and Engineering: A **396** (1-2), 61-69 (2005).

120.	Y. Iida and S. Ozaki, Journal of the American Ceramic Society **44** (3), 120-127 (1961).

121.	M. S. P. Francisco and V. R. Mastelaro, Chemistry of Materials **14** (6), 2514-2518 (2002).

122.	Y.-H. Zhang and A. Reller, Materials Science and Engineering: C **19** (1-2), 323-326 (2002).

123.	G. Bond, Journal of Catalysis **57** (3), 476-493 (1979).

124.	E. Setiawati and K. Kawano, Journal of Alloys and Compounds **451** (1-2), 293-296

(2008).

125.   R. A. Eppler, Journal of the American Ceramic Society **70** (4), C-64-C-66 (1987).

126.   K. Okada, N. Yamamoto, Y. Kameshima, A. Yasumori and K. J. D. MacKenzie, Journal of the American Ceramic Society **84** (7), 1591-1596 (2004).

127.   J. Kim, K. C. Song, S. Foncillas and S. E. Pratsinis, Journal of the European Ceramic Society **21** (16), 2863-2872 (2001).

128.   M. K. Akhtar, S. E. Pratsinis and S. V. R. Mastrangelo, Journal of the American Ceramic Society **75** (12), 3408-3416 (1992).

129.   Z. M. Shi, L. Yan, L. N. Jin, X. M. Lu and G. Zhao, Journal of Non-Crystalline Solids **353** (22-23), 2171-2178 (2007).

130.   K.-N. P. Kumar, D. J. Fray, J. Nair, F. Mizukami and T. Okubo, Scripta Materialia **57** (8), 771-774 (2007).

131.   C. Li, L. Shi, D. Xie and H. Du, Journal of Non-Crystalline Solids **352** (38-39), 4128-4135 (2006).

132.   S. Rajesh Kumar, S. C. Pillai, U. S. Hareesh, P. Mukundan and K. G. K. Warrier, Materials Letters **43** (5-6), 286-290 (2000).

133.   S. Perera and E. G. Gillan, Chemical communications (48), 5988-5990 (2005).

134.   S. Hishita, I. Mutoh, K. Koumoto and H. Yanagida, Ceramics International **9** (2), 61-67 (1983).

135.   S. Sharma, S. Chaudhary, S. C. Kashyap and S. K. Sharma, Journal of Applied Physics **109** (8), 083905 (2011).

136.   G. Glaspell and A. Manivannan, Journal of Cluster Science **16** (4), 501-513 (2005).

137.   J. Criado and C. Real, Journal of the Chemical Society, Faraday Transactions 1: Physical Chemistry in Condensed Phases **79** (12), 2765 (1983).

138.   S. J. Smith, R. Stevens, S. Liu, G. Li, A. Navrotsky, J. Boerio-Goates and B. F. Woodfield, American Mineralogist **94** (2-3), 236-243 (2009).

139.   H. Zhang and J. F. Banfield, Journal of Materials Chemistry **8** (9), 2073-2076 (1998).

140.   A. Navrotsky and O. J. Kleppa, Journal of the American Ceramic Society **50** (11), 626-626 (1967).

141.   N. Savage and M. S. Diallo, Journal of Nanoparticle Research **7** (4-5), 331-342 (2005).

142.   N. M. Mahmoodi and M. Arami, Journal of photochemistry and photobiology. B, Biology **94** (1), 20-24 (2009).

143.   K. Vinodgopal, I. Bedja, S. Hotchandani and P. V. Kamat, Langmuir **10** (6), 1767-

1771 (1994).

144.   M. A. Rauf and S. S. Ashraf, Chemical Engineering Journal **151** (1-3), 10-18 (2009).

145.   R. Brahimi, Y. Bessekhouad, A. Bouguelia and M. Trari, Journal of Photochemistry and Photobiology A: Chemistry **194** (2-3), 173-180 (2008).

146.   I. K. Konstantinou and T. A. Albanis, Applied Catalysis B: Environmental **49** (1), 114 (2004).

147.   C. Renz, Helvetica Chimica Acta **4** (1), 961-968 (1921).

148.   C. F. Goodeve and J. A. Kitchener, Transactions of the Faraday Society **34**, 570 (1938).

149.   A. E. Jacobsen, Industrial & Engineering Chemistry **41** (3), 523-526 (1949).

150.   A. Fujishima, X. Zhang and D. Tryk, Surface Science Reports **63** (12), 515-582 (2008).

151.   M. C. Markham and K. J. Laidler, The Journal of Physical Chemistry **57** (3), 363-369 (1953).

152.   T. R. Rubin, J. G. Calvert, G. T. Rankin and W. MacNevin, Journal of the American Chemical Society **75** (12), 2850-2853 (1953).

153.   R. E. Stephens, B. Ke and D. Trivich, The Journal of Physical Chemistry **59** (9), 966-969 (1955).

154.   W. R. Hindson and P. G. Kelly, Nature **177** (4522), 1241-1242 (1956).

155.   D. R. Kennedy, M. Ritchie and J. Mackenzie, Transactions of the Faraday Society **54**, 119 (1958).

156.   M. Kato S, Kogyo Kagaku Zasshi **67**, 9 (1964).

157.   S. N. Frank and A. J. Bard, Journal of the American Chemical Society **99** (1), 303-304 (1977).

158.   G. N. Schrauzer and T. D. Guth, Journal of the American Chemical Society **99** (22), 7189-7193 (1977).

159.   O. J. Fujishima A, Yamashita T, et al., Photomed Photobiol, **8**, 2 (1986).

160.   B. O'Regan and M. Grätzel, Nature **353** (6346), 737-740 (1991).

161.   R. Wang, K. Hashimoto, A. Fujishima, M. Chikuni, E. Kojima, A. Kitamura, M. Shimohigoshi and T. Watanabe, Nature **388** (6641), 431-432 (1997).

162.   S. Watson, D. Beydoun and R. Amal, Journal of Photochemistry and Photobiology A: Chemistry **148** (1-3), 303-313 (2002).

163.   R. S. Sonawane, B. B. Kale and M. K. Dongare, Materials Chemistry and Physics **85** (1), 52-57 (2004).

164.   L. Diamandescu, F. Vasiliu, D. Tarabasanu-Mihaila, M. Feder, A. M. Vlaicu, C. M. Teodorescu, D. Macovei, I. Enculescu, V. Parvulescu and E. Vasile, Materials Chemistry and Physics **112** (1), 146-153 (2008).

165.   T.-Y. Lai and W.-C. Lee, Journal of Photochemistry and Photobiology A: Chemistry **204** (2-3), 148-153 (2009).

166.   O. R. S. da Rocha, R. F. Dantas, M. M. M. B. Duarte, M. M. L. Duarte and V. L. da Silva, Chemical Engineering Journal **157** (1), 80-85 (2010).

167.   C. Chen, Z. Wang, S. Ruan, B. Zou, M. Zhao and F. Wu, Dyes and Pigments **77** (1), 204-209 (2008).

168.   Y. Zhao, C. Li, X. Liu, F. Gu, H. L. Du and L. Shi, Applied Catalysis B: Environmental **79** (3), 208-215 (2008).

169.   V. Mirkhani, S. Tangestaninejad, M. Moghadam, M. H. Habibi and A. Rostami-Vartooni, J Iran Chem Soc **6** (3), 578-587 (2009).

170.   W. Choi, A. Termin and M. R. Hoffmann, The Journal of Physical Chemistry **98** (51), 13669-13679 (1994).

171.   Z. M. El-Bahy, A. A. Ismail and R. M. Mohamed, Journal of hazardous materials **166** (1), 138-143 (2009).

172.   J. Xu, Y. Ao and D. Fu, Applied Surface Science **256** (3), 884-888 (2009).

173.   X. Z. Shen, Z. C. Liu, S. M. Xie and J. Guo, Journal of hazardous materials **162** (2-3), 1193-1198 (2009).

174.   X. Yang, F. Ma, K. Li, Y. Guo, J. Hu, W. Li, M. Huo and Y. Guo, Journal of hazardous materials **175** (1-3), 429-438 (2010).

175.   X. H. Wang, J. G. Li, H. Kamiyama, Y. Moriyoshi and T. Ishigaki, Journal of Physical Chemistry B **110** (13), 6804-6809 (2006).

176.   M. Yin, Z. Li, J. Kou and Z. Zou, Environmental science & technology **43** (21), 8361-8366 (2009).

177.   M. Saquib and M. Muneer, Journal of Environmental Science and Health, Part A **38** (11), 2581-2598 (2003).

178.   H. Taoda, Research on Chemical Intermediates **34** (4), 417-426 (2008).

179.   T.-H. Bui, M. Karkmaz, E. Puzenat, C. Guillard and J.-M. Herrmann, Research on Chemical Intermediates **33** (3-5), 421-431 (2007).

180.   E. L. R. Prairie M R, Martinez S L., Technology for the nineties. In: Second International Symposium. Lancaster: Technomic Publishing Company, 1994 (1994).

181.   L. Pereira, R. Pereira, C. S. Oliveira, L. Apostol, M. Gavrilescu, M. N. Pons, O.

Zahraa and M. M. Alves, Photochemistry and photobiology **89** (1), 33-39 (2013).

182.   R. Mohammadi and M. Mohammadi, Desalination and Water Treatment **57** (24), 11317-11325 (2015).

183.   F. Valentini and G. Palleschi, Analytical Letters **41** (4), 479-520 (2008).

184.   H. Dislich, Journal of Non-Crystalline Solids **80** (1-3), 115-121 (1986).

185.   S. R. G. J. B. Blum, Journal of Materials Science **20** (12), 5 (1985).

186.   L. L. Hench and J. K. West, Chemical reviews **90** (1), 33-72 (1990).

187.   N. T. Thanh, N. Maclean and S. Mahiddine, Chemical reviews **114** (15), 7610-7630 (2014).

188.   R. Guinebretière, (2010).

189.   R. A. Spurr and H. Myers, Analytical Chemistry **29** (5), 760-762 (1957).

190.   K. Sakurai and M. Mizusawa, Anal Chem **82** (9), 3519-3522 (2010).

191.   K. Sakurai, Natur Materials **8** (2009).

192.   H. E. Chao, Y. U. Yun, H. U. Xingfang and A. Larbot, Journal of the European Ceramic Society **23** (9), 1457-1464 (2003).

193.   P. Singla, M. Sharma, O. P. Pandey and K. Singh, Applied Physics A **116** (1), 371-378 (2013).

194.   K. Ubonchonlakate, L. Sikong and F. Saito, Procedia Engineering **32**, 656-662 (2012).

195.   K. Gupta, R. P. Singh, A. Pandey and A. Pandey, Beilstein journal of nanotechnology **4**, 345-351 (2013).

196.   M. B. Suwarnkar, R. S. Dhabbe, A. N. Kadam and K. M. Garadkar, Ceramics International **40** (4), 5489-5496 (2014).